Bulk and surface acoustic wave phenomena in crystals: Observation and interpretation

A.G. Every [a,*], A.A. Maznev [b], W. Grill [c], M. Pluta [d], J.D. Comins [a], O.B. Wright [e], O. Matsuda [e], W. Sachse [f], J.P. Wolfe [g]

[a] School of Physics, University of the Witwatersrand, PO Wits 2050, South Africa
[b] Department of Chemistry, Massachusetts Institute of Technology, Cambridge, MA 02139, USA
[c] Institut fur Experimentelle Physik II, Universitaet Leipzig, Linnestr. 5, D-04103 Leipzig, Germany
[d] Institute of Physics, Wrocław University of Technology, Wyb. Wyspiańskiego 27, 50-370 Wrocław, Poland
[e] Division of Applied Physics, Faculty of Engineering, Hokkaido University, Sapporo 060-8628, Japan
[f] Sibley School of Mechanical and Aerospace Engineering, Cornell University, Ithaca, NY 14953, USA
[g] Department of Physics, University of Illinois at Urbana-Champaign, Urbana, IL 61801, USA

HIGHLIGHTS

- We review acoustic wave phenomena in crystals.
- We place emphasis on phonon imaging, laser ultrasound and acoustic microscopy.
- We explore bulk and surface wave phenomena in near and far fields.
- We treat slowness and wave surfaces, acoustic axes and polarization singularities.

ARTICLE INFO

ABSTRACT

Crystal acoustics is a field that has engaged the attention of theoreticians and experimentalists alike for decades and more. Many striking effects have been revealed, and elegant analytical techniques applied to their interpretation. This article is oriented towards the experimental aspects of the field and the interpretation of the phenomena that have been observed. Particular attention is given to reviewing the techniques that have probed the intricacy of acoustic wave propagation in crystals, including phonon imaging, laser- and capillary-fracture-generated ultrasound, transmission acoustic microscopy and surface Brillouin scattering, and a selection of results obtained with these techniques is presented. Some of these studies pertain to bulk waves and others to surface acoustic waves. The interpretation of far-field observations is carried out within the ray approximation, and elastodynamic Green's functions are invoked in the interpretation of near-field results. Extensive use is made of the acoustic-slowness and wave surfaces, in particular features such as acoustic axes, with their attendant polarization singularities, and folds in the wave surface.

Crystal acoustics is a world of new and beautiful physical phenomena, and elegant theoretical constructs, which have both intrinsic aesthetic value and potential for applications.

[Vladimir Alshits, Sov. Phys. Acoust. 38 (1993) 614]

* Corresponding author. Tel.: +27 11 717 6823; fax: +27 11 717 6879.
  E-mail address: arthur.every@wits.ac.za (A.G. Every).

1. Introduction

This article, in the form of a review, provides experimental support for Vladimir Alshits' assertion that "Crystal acoustics is a world of new and beautiful physical phenomena" [1]. In the interpretation and modeling of the experimental phenomena to be discussed, use will be made of some of the "elegant theoretical constructs" which he and others have developed. The experimental techniques that reveal these phenomena will be described, and results of measurements will be presented. Some of the techniques, such as phonon imaging, relate to far-field effects which are well accounted for on the basis of the ray approximation. Other techniques, such as capillary-fracture generation of displacement waveforms and transmission acoustic microscopy (TAM) imaging, relate to the near or intermediate field, and time – or frequency – domain elastodynamic Green's functions are invoked in their interpretation. Some of the techniques are concerned with bulk waves and others with surface acoustic waves (SAW). In spite of the diversity of approaches, there is a unity and coherence in the results that emerge. A recurring theme in the discussion is that of acoustic axes and the polarization singularities that attach to them. This is a topic that Vladimir Alshits has contributed importantly to, and which has widespread experimental ramifications.

It is not possible in this article to give complete coverage to all the striking crystal acoustics phenomena there are. We have had to be selective in choosing topics for inclusion, limiting the scope of the article to linear elasticity of continuous media. In particular, we do not venture into the currently very active field of phononic crystals.

Most of the results that will be presented in this paper pertain to "normal" crystals such as Si, GaAs, CaF$_2$ and Zn, i.e. materials which do not have special values of elastic constants that would endow them with non-generic behavior, and which do not inhabit remote regions of parameter space where exceptional behavior is to be encountered. Some results are, however, included for the exceptionally anisotropic crystal TeO$_2$. Statements will be made about crystalline solids without extensive qualification, but these should not be interpreted as applying to all materials. Thus, for example, we will speak loosely of longitudinal and transverse wave modes, recognizing that most crystals exhibit quasi-longitudinal and quasi-transverse modes of mixed character where one or the other polarization may be dominant. Rather than explore all mathematically possible types of behavior in crystal acoustics, this paper will illustrate some of the more interesting physical phenomena with materials that are readily available.

This paper is structured as follows: In Section 2 we provide a brief introduction into the theoretical background of crystal acoustics, with discussion of the wave equation, the ray surface and the acoustic slowness surface together with the polarization singularities it displays at acoustic axes. In Section 3 we treat bulk wave phenomena, encompassing far- and near-field effects, treated respectively on the basis of the ray approximation and in terms of elastodynamic Green's functions. We then discuss energy focusing and its observation with phonon imaging and laser-scan imaging, and afterwards touch on the phenomenon of external conical refraction. We then discuss TAM results within the context of frequency-domain Green's functions, and treat capillary-fracture-generated waveforms and the wave-arrival singularities they contain on the basis of time-domain Green's functions. In Section 4 we cover guided waves at surfaces and supported layers, again encompassing far- and near-field phenomena. Effects covered include surface Brillouin scattering, birefringence of SAW, phonon focusing of SAW, frequency and time-domain surface response functions and the observation of SAW wave-front propagation. In Section 5 we present the conclusions.

2. Theoretical preliminaries — the acoustic slowness and wave surfaces

2.1. The wave equation

The effects described in this paper derive from the elastic wave equation [2–4]

$$\rho \frac{\partial^2 u_i}{\partial t^2} = c_{ijkl} \frac{\partial^2 u_k}{\partial x_j \partial x_l}, \tag{1}$$

for an ideal elastically anisotropic solid, $\mathbf{u}(\mathbf{x}, t)$ being the particle displacement field, ρ the density, and c_{ijkl} the elastic modulus tensor of the solid. Eq. (1) admits plane wave solutions of the form

$$u_i = U_i \exp[i(\mathbf{k} \cdot \mathbf{x} - \omega t)], \tag{2}$$

with the unit polarization vector, $\mathbf{U}$, wave vector, $\mathbf{k} = \frac{2\pi}{\lambda} \mathbf{n}$ (where λ is the wavelength and $\mathbf{n}$ the wave normal), and the angular frequency, ω, being governed by the Christoffel equations
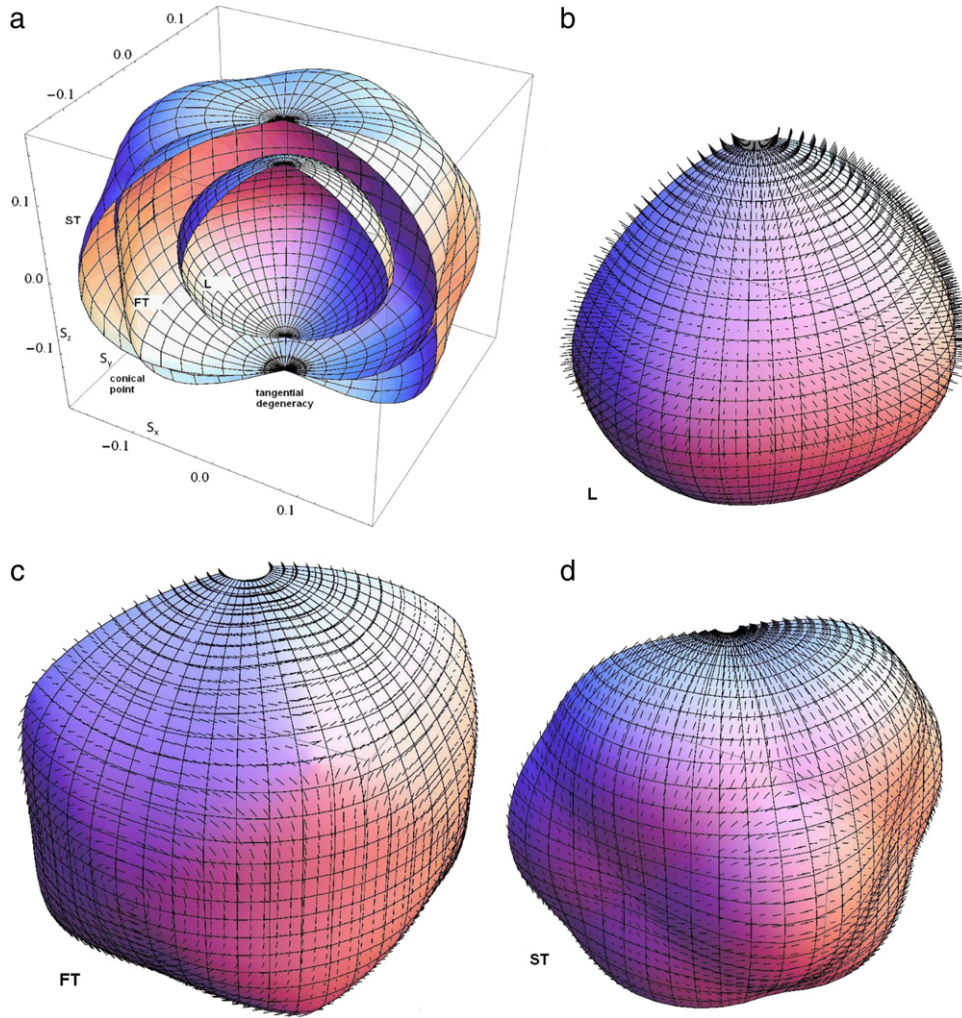
$$(c_{ijkl} k_j k_l - \rho \omega^2 \delta_{ik}) U_k = 0; \quad i = 1, 2, 3. \tag{3}$$

The corresponding secular equation

$$D(\mathbf{k}, \omega) = |c_{ijkl} k_j k_l - \rho \omega^2 \delta_{ik}| = 0, \tag{4}$$

represents the dispersion relation of the medium, and expresses a linear dependence of ω on $k = |\mathbf{k}|$. The iso-frequency surfaces it defines are all identical in shape, and scale in size with ω. Division of (4) by k^6 yields the equation

$$|c_{ijkl} n_j n_l - \rho v^2 \delta_{ik}| = 0, \tag{5}$$

Fig. 1. Slowness surface of silicon crystal, (a) showing all 3 sheets, and (b), (c) and (d) showing individually the L-, FT- and ST sheets with the mode-polarization fields superimposed. The scale in (a) is given in μs/mm.

for the phase velocity $v = \omega/k$. It is cubic in v^2, and the three solutions that emerge correspond to mutually orthogonal wave polarizations. The one belonging to the largest value of v is in general quasi-longitudinal (L) and the other two are quasi-transverse (T), and are referred to as the fast-transverse (FT) and slow-transverse (ST) modes.
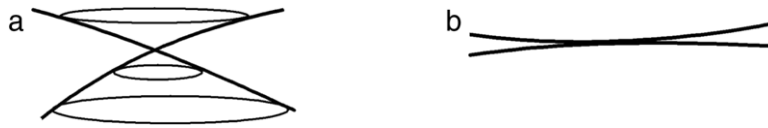
2.2. The slowness surface

The acoustic slowness surface plays a central role in the analysis of many crystal acoustics phenomena, including phonon focusing, reflection and transmission at surfaces, and surface and interfacial waves. It is a centrosymmetric surface of three sheets representing the directional dependence of the acoustic slowness or inverse phase velocity $s = 1/v$, and as such it is the locus of slowness vectors $\mathbf{s} = \mathbf{k}/\omega = \mathbf{n}/v$ with respect to $\mathbf{n}$. The slowness surface is identical in shape to the constant frequency surfaces, differing only in scale. The equation for the slowness surface is obtained by dividing Eq. (4) by ω^6 to yield

$$S(\mathbf{s}) = |c_{ijkl}s_j s_l - \rho\delta_{ik}| = 0, \tag{6}$$

and is of degree 6 in the components of $\mathbf{s}$.

Fig. 1(a) depicts the slowness surface of the cubic crystal silicon. As is commonly but not invariably the case, the L slowness sheet lies entirely within and separate from the T sheets. The FT and ST sheets meet in a number of isolated directions known as acoustic axes, which, for cubic crystals, lie along the ⟨100⟩ and ⟨111⟩ crystallographic axes of 4-fold and 3-fold symmetry respectively. For crystals of lower than cubic or hexagonal symmetry, acoustic axes are not necessarily confined to symmetry directions. The elastic moduli of hexagonal crystals conform to transverse isotropy and, depending on the values of the moduli, the transverse slowness sheets may have line intersections encircling the zonal axis, as discussed later.

Fig. 2. Schematic representation of transverse-mode slowness surface in the region of (a) a conical point, with $n = \pm\frac{1}{2}$, and (b) a touching contact, with $n = \pm 1$ degeneracies.
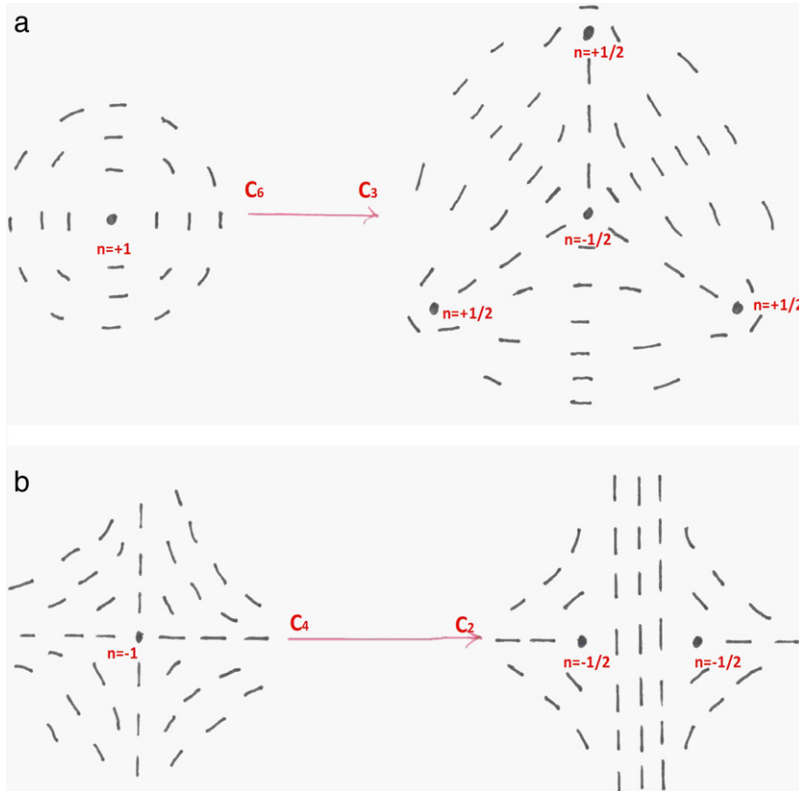

Fig. 3. Conservation of topological charge $\sum n$ in the splitting of polarization singularities with lowering of a medium's symmetry: (a) effect of lowering of 6-fold C_6 to 3-fold C_3 symmetry on a $n = 1$ singularity [8], (b) effect of lowering of 4-fold C_4 to 2-fold C_2 symmetry on a $n = -1$ singularity.

Fig. 1(b)–(d) show the L-, FT- and ST slowness sheets of Si individually with the mode-polarization fields superimposed. Singularities appear in the transverse-mode polarization fields in the neighborhoods of the acoustic axes. The L-mode polarization field is close to radial in all directions and contains no singularities.

Excluding the line intersections of transverse isotropy, acoustic axes are of two types [5–11]: conical points (conical degeneracies), where the two slowness sheets meet in the form of a double cone, and touching contacts (tangential degeneracies), as shown in Fig. 2. In the neighborhood of an acoustic axis the orthogonal polarization fields of the two slowness sheets contain a rotational singularity. Its nature is such that in tracing a small path around the acoustic axis on either sheet, the polarization rotates by $2\pi n$, where n is known as the Poincaré index for the singularity [8–10].

For conical points located on a 3-fold symmetry axis, $n = -\frac{1}{2}$, whereas for a non-symmetry direction conical point there are two possibilities, $n = \frac{1}{2}$ and $n = -\frac{1}{2}$. A conical point is structurally stable, in the sense that it does not require symmetry for its existence, and a perturbation to the elastic moduli may cause an isolated conical point to move but not to disappear.

For touching contacts, $n = 1$ or $n = -1$. The $n = 1$ singularities generically only occur along 4- and 6-fold symmetry axes, and $n = -1$ singularities only occur along 4-fold symmetry axes. These $n = \pm 1$ singularities are structurally unstable, in that a lowering of the symmetry causes them to split into conical-point singularities with conservation of total "topological charge" $\sum n$, as illustrated in Fig. 3. A reduction of symmetry can occur in a medium for the case of a phase transition, as for the example of quartz which changes from the hexagonal β phase to the trigonal α phase as the temperature is lowered below 573 °C.
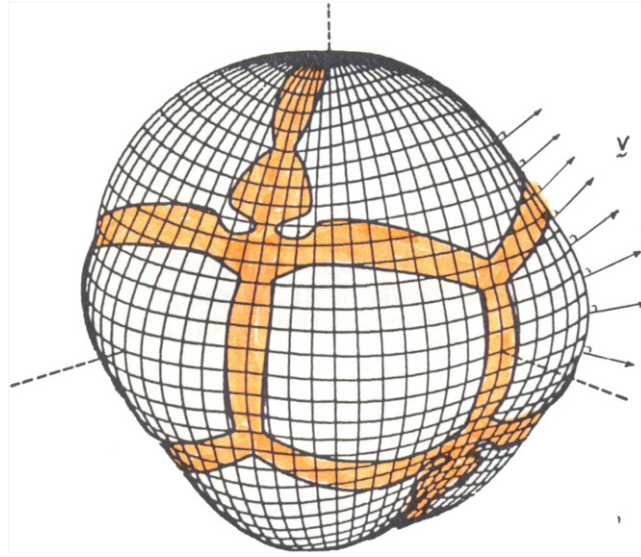
Fig. 4. ST sheet of the slowness surface of sapphire, and a few rays.

2.3. Group velocity and ray surface

The velocity characterizing signal or energy propagation in the far field is the group or ray velocity. It is the velocity with which a wave packet propagates, and is given by

$$\mathbf{V} = \left(\frac{\partial \omega}{\partial k_1}, \frac{\partial \omega}{\partial k_2}, \frac{\partial \omega}{\partial k_3} \right) = \nabla_k \omega(\mathbf{k}). \tag{7}$$

It can deviate significantly in direction from the wave normal. It follows from the defining equation that the group velocity is normal to the iso-frequency and slowness surfaces. This is illustrated in Fig. 4. Since ω is a homogeneous function of degree 1 in $\mathbf{k}$, it follows from Euler's theorem that

$$k_i \frac{\partial \omega}{\partial k_i} = \omega, \quad i.e. \ \mathbf{k} \cdot \mathbf{V} = \omega, \ \mathbf{n} \cdot \mathbf{V} = v, \ \mathbf{s} \cdot \mathbf{V} = 1. \tag{8}$$

From the slowness surface equation,

$$\mathbf{V} = \frac{\nabla_s S(\mathbf{s})}{\mathbf{s} \cdot \nabla_s S(\mathbf{s})}. \tag{9}$$

The ray surface is the locus of tips of ray vectors $\mathbf{V}$ for all wave normals $\mathbf{n}$. It can take on physical form, in that it is the surface on which wave-arrival singularities with their concentration of energy propagate outwards from a sudden point disturbance in a medium. It is in general a more complicated surface than the slowness surface, as one can see in the example of GaAs in Fig. 5, with the transverse sheets commonly displaying folds with sharp cuspidal-shaped edges. The projective relationship between the slowness and ray surfaces facilitates an understanding of the complex features of the ray surface. The shaded areas on the slowness surface in Fig. 4 are saddle-shaped regions of negative Gaussian curvature, the rest of the surface being convex and of positive Gaussian curvature. Parabolic lines, i.e. lines of zero Gaussian curvature, separate these regions. Points on a parabolic line of the slowness surface map onto a fold in the wave surface, which because of the vanishing of the Jacobian of the mapping, represents a line of accumulation of the rays. The consequences of this are discussed in the next section.

Because the equation of the slowness surface is of degree 6, the inner sheet cannot be concave at any point, and so the inner sheet of the ray surface does not exhibit folds. This restriction does not apply to piezoelectric crystals, for which the slowness surface equation is of degree 8, and the inner ray sheet of, for example the strongly piezoelectric crystal Rochelle salt, is indeed folded [12].

3. Bulk wave phenomena

3.1. Energy focusing in the ray approximation — phonon imaging

The variation of the curvature of the slowness surface has a profound effect on the directional dependence of the acoustic energy flux radiated by a point source in an anisotropic solid. We consider here how this arises in the context of the ray
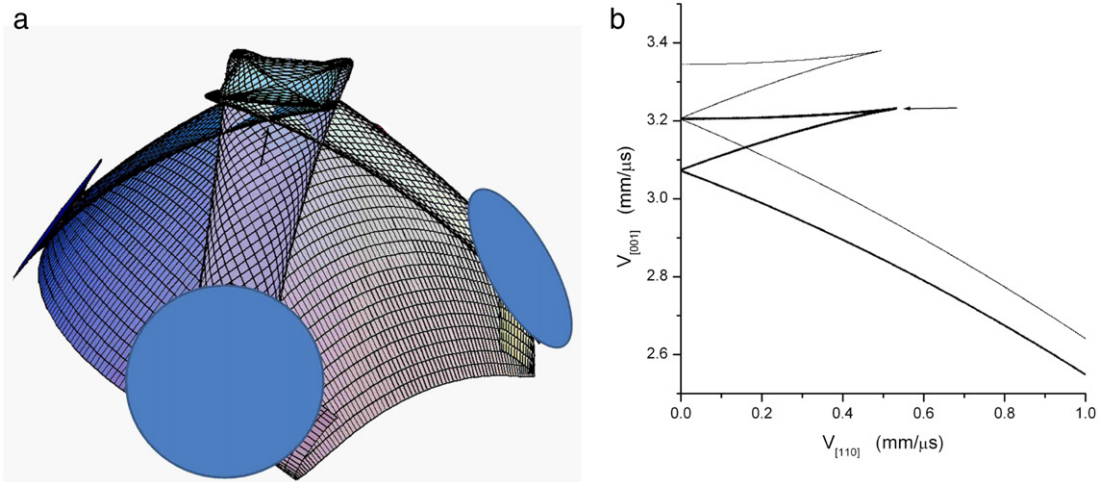
Fig. 5. Portion of the multiply-folded ST sheet of the ray surface of GaAs, (a) 3D view, and (b) plane-sectioned view. The arrows in the two diagrams are directed at the same velocity point where two sharp folds of the ray surface intersect. The flat disks are the "lids" of internal conical refraction [6,13,14].

approximation, assuming that the radiation is incoherent and is composed of an omni-directional distribution of $\mathbf{k}$ (or $\mathbf{s}$) vectors. Referring to Fig. 4, the rays pointing out of this slowness surface can be taken to represent some of the ray vectors making up the acoustic flux. It is evident that where the curvature of the slowness surface is small, the ray vectors are strongly bunched together in direction, and consequently the energy flux in that direction is great, and vice versa. This effect is known as energy enhancement or phonon focusing, and a useful measure for it is the Maris phonon enhancement factor [15,16]

$$A = \left| \frac{\delta \Omega_s}{\delta \Omega_V} \right|, \tag{10}$$

in which $\delta \Omega_s$ is the solid angle subtended by an infinitesimal cone of slowness vectors and $\delta \Omega_V$ is the solid angle subtended by their associated ray vectors. From the geometry of surfaces it is readily established that [17,18]

$$A = \left| s^3 V K \right|^{-1}; \quad K = L_1 L_2, \tag{11}$$

where K is the Gaussian curvature and L_1 and L_2 are the principal curvatures of the slowness surface. The relative variation of s and V is in general modest in comparison with K, and it is K which is mainly responsible for the pronounced variation of A that occurs. We will see later that the stationary phase approximation to the elastodynamic response leads to the same dependence on curvature as in Eq. (11).

Energy flux enhancement is revealed most vividly with the phonon imaging technique [19], the underlying principle of which is as follows. The thermal energy of (non-metallic) solids can in large measure be ascribed to high frequency acoustic waves $> 10^{11}$ Hz, which at low temperatures reveal the effects of quantization. The quantum of energy is the phonon, which can loosely be thought of as an acoustic wave packet. Whereas at high temperatures there is considerable phonon scattering and heat flow is as a consequence diffusive, at low temperatures there are few ambient phonons to scatter from, and injected phonons travel ballistically through the medium. The principle of the phonon imaging technique is depicted in Fig. 6(a). A laser pulse is used to heat a small spot on a crystal maintained at an ambient temperature near absolute zero. The phonons thereby injected travel unimpeded at their individual group velocities to the opposite face of the sample where they are detected by a bolometer. By raster scanning the laser spot over the front surface, one builds up an image portraying the directional dependence of the phonon flux. Fig. 6(b) shows a measured image for a (100)-oriented silicon crystal [39] and 6(c) the corresponding calculated image. They are in excellent agreement.

A common point of departure in the computer simulations of phonon images is to assume that the phonons emanating from the heat source have a uniform distribution of wave normals. The group velocities for a large number of normals are computed, and the points where these meet the viewing surface are sorted into a 2D array of bins. The result is often presented as a gray scale image, such as the one shown in Fig. 6(c).

The most striking feature of phonon images is the pattern of caustics they contain. These intense bands are associated with parabolic lines on the slowness surface and folds in the wave surface. The vanishing of K on these lines results in the energy flux being infinite in the ideal case. Caustics are essentially a far field effect, and can be classified on the basis of elementary catastrophe theory [20]. The patterns they form for different crystal symmetries and degrees of anisotropy have been extensively studied experimentally and theoretically by a number of authors, and the existence of line, cusp, swallowtail, butterfly and umbilic caustics has been noted [17].

The existence of phonon caustics for a medium does not in general require a particularly high degree of anisotropy; in non-hexagonal crystals their existence is guaranteed by the presence of conical points. In the vicinity of a conical point at
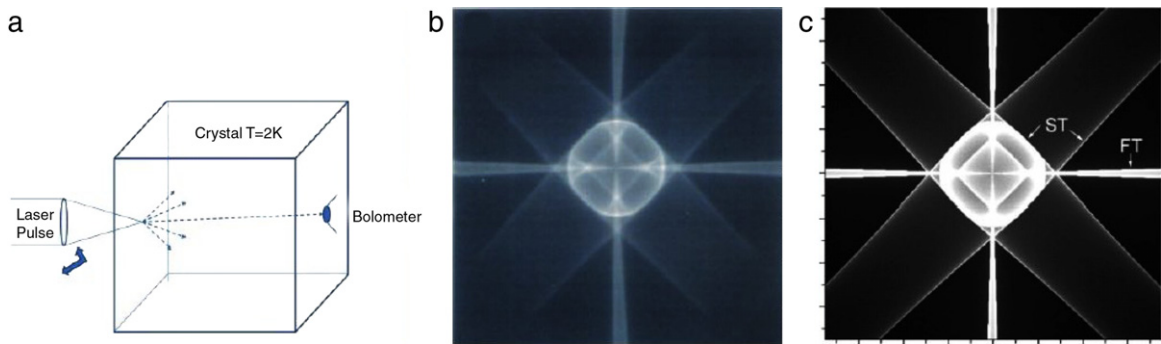
Fig. 6. (a) The phonon imaging principle, and (b) measured [39] and (c) calculated phonon images of Si(001). Time gating has been used to capture only the transverse phonons.
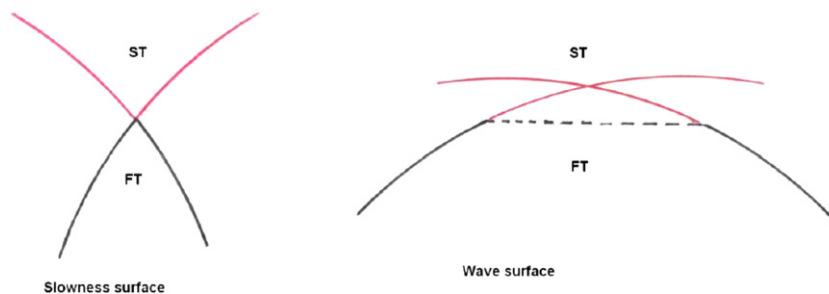
Fig. 7. Internal conical refraction as the origin of an "anti-caustic" on which the ST and FT wave sheets meet.

least one of the principal curvatures of the ST slowness sheet must be negative, and since this sheet must elsewhere possess convex regions to be a closed surface, there must be parabolic lines on that surface and hence caustics [17]. For generic values of elastic constants, all cubic and lower-symmetry crystals possess conical points, however small the degree of anisotropy, and hence they display phonon caustics. For purely elastic media, because the L (inner) slowness sheet is entirely convex, the L modes do not form caustics.

3.1.1. Anti-caustic for conical point

Points on the slowness surface in the immediate neighborhood of a conical point map onto an ellipse (or circle for a 3-fold symmetry axis) in the ray surface at which the FT and ST ray sheets meet, an effect known as internal conical refraction. One of the principle curvatures of the slowness surface diverges at the conical point, so the phonon enhancement goes to zero on that ellipse (or circle) in the wave surface, which can thus be regarded as an "anti-caustic". (The plane surface bounded by the ellipse and known as the "lid", the dashed line in Fig. 7 and the flat disks in Fig. 5, shows up as a wave-arrival singularity of low order in elastodynamic Green's functions [13,14], but plays no role in the ray approximation.)

3.1.2. Collision between a caustic and anti-caustic

For a certain domain of cubic-crystal elastic constants, the slowness surface is shaped in such a way that there is a parabolic line which weaves its way back and forth through the conical point between the ST and FT sheets, enclosing 3 petal-shaped regions in the ST sheet where both principal curvatures are negative, and also enclosing three similar-shaped but 60°-rotated regions on the FT sheet where the principal curvatures are both positive [17,21]. As a result of this, there is a fold and an associated caustic, part of which lies on the ST wave sheet and part on the FT sheet. The caustic meets the circular anti-caustic tangentially as it passes between the two sheets, fading in intensity to zero as it does so. This is exemplified in the measured and calculated phonon images of calcium fluoride shown in Fig. 8.

The phonons comprising thermal energy and participating in phonon imaging are incoherent, span a broad spectrum, and do not in the first instance show any marked preference for polarization. This is not the case for elastic waves excited coherently by thermal or mechanical means as we show in the remainder of Section 3.

3.2. Laser-generated ultrasound waveforms

There have been numerous reports of laser generated ultrasound measurements carried out on silicon, zinc and other single crystals at ambient temperatures. In the standard approach [23,24], as depicted in Fig. 9, a focused Q-switched laser delivers a heat pulse to a small region on the surface of a specimen, causing transient acoustic waves to be launched into the specimen. The wave field is measured on the opposite face using laser interferometry, or a small-aperture piezoelectric or
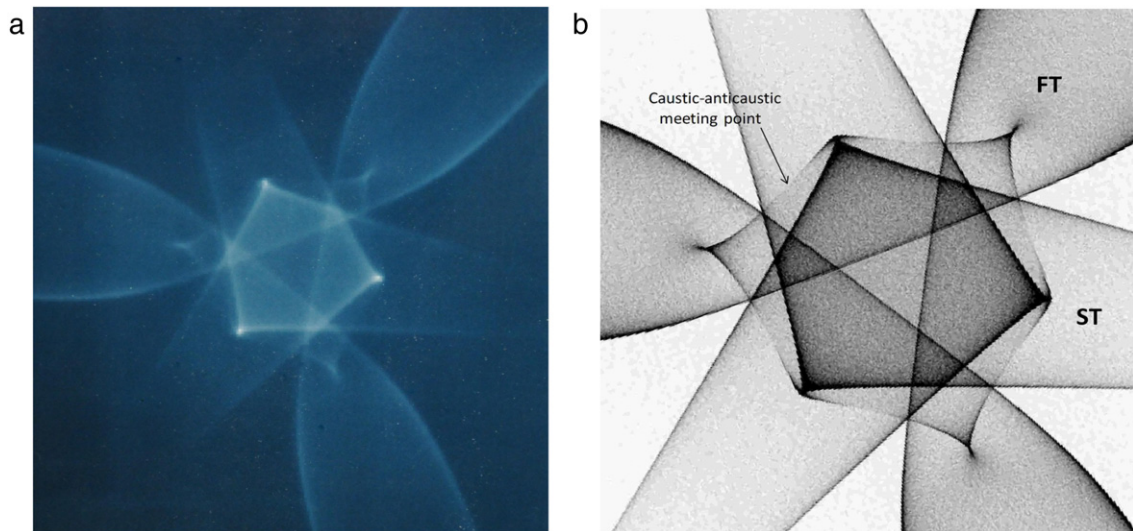
Fig. 8. (a) Phonon image of CaF_2 measured by Hurley and Wolfe [22], showing caustic–anti-caustic "collision", and (b) calculated focusing pattern for the central region.
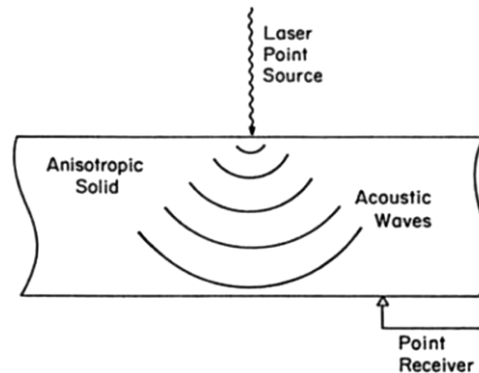

Fig. 9. Principle of laser-scan imaging.

capacitive transducer, which senses the normal displacement of the surface. Note that it is the thermally generated acoustic wave that is detected, not the thermal phonons making up the heat pulse as is the case in phonon imaging. At low laser intensity the thermoacoustic generation mechanism usually predominates, whereby the rapid rise in temperature at the surface brings about a sudden localized axial-stress field within the surface, resulting in acoustic radiation [25]. In silicon at low laser fluences, the excitation of free carriers generates the stress field through the deformation potential [26]. At higher intensities, material is ablated from the surface, and this gives rise to an impulsive reaction force normal to the surface [25,26]. The generation and detection processes are both to a high degree axisymmetric in form, and only waves with a significant sagittal component to their polarization feature in the observations.

Fig. 10(a) shows a scan image obtained by Every and Sachse [24] on a 10-mm thick (001)-oriented silicon single crystal by stacking together a large number of displacement waveforms measured for a fixed detector position and a closely-spaced set of excitation points along the [100] direction in the upper surface. The small aperture "pinducer" used in the detection is prone to ringing, and it is only the signal onsets triggered by wave arrivals, which travel at the group velocity and deliver concentrated acoustic energy, which are of concern here. Fig. 10(b) shows the theoretical wave arrivals obtained by assuming a uniform distribution of wave normals **n**, and plotting as points the arrival times of those rays that come within the detector aperture for each value of source position x. The calculated scan image features the first L and ST wave arrivals, their head wave (HW), and the arrivals of various mode-conversion sequences for passage of the wave field three and five times through the sample. The multi-pass and head waves are calculated using standard procedures for dealing with reflection in anisotropic solids. These various wave arrivals are all in good agreement with the signal onsets in the measured scan image. There is no discernible presence of FT single- or multi-pass waves, or any mode conversion sequence or head wave involving FT waves. The reason for this is that, owing to the polarization singularity in the [001] direction, the FT waves are almost perfectly shear-horizontally (SH) polarized for this configuration (see scan line A on Fig. 10(c) and (d)), and are therefore uncoupled from the axisymmetric mode of excitation and detection.
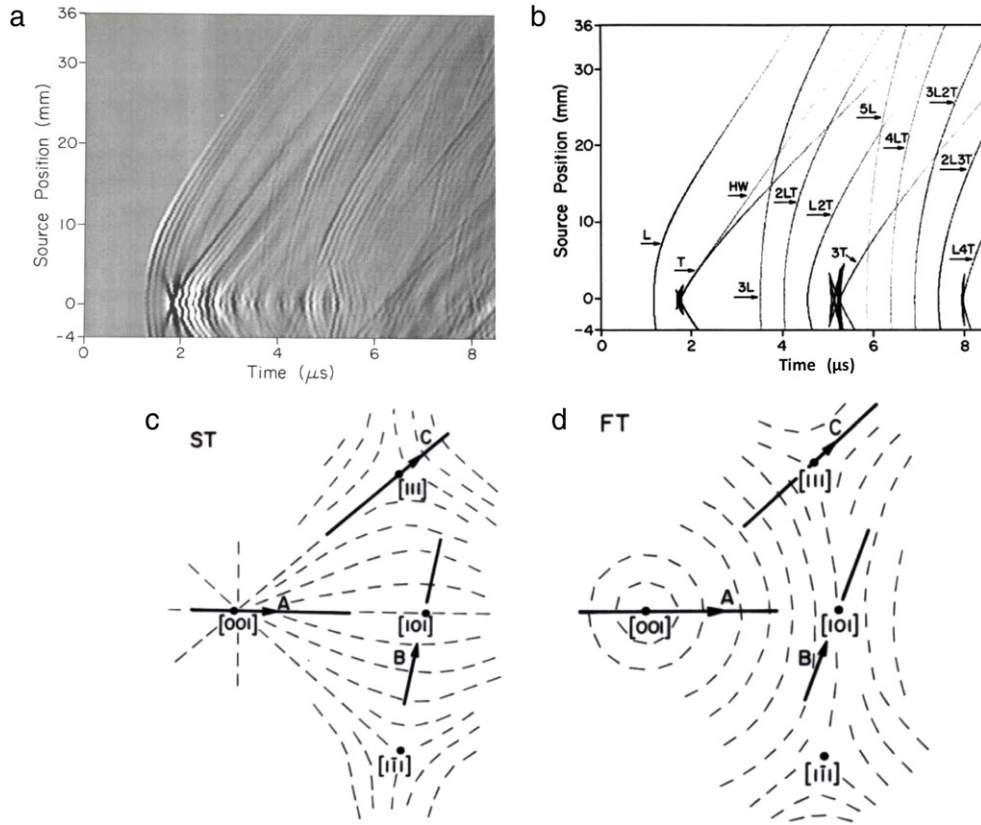
Fig. 10. Scan imaging of Si (001): (a) measured, and (b) calculated images. The excitation, whether thermoelastic, ablative, or through free carrier excitation, is axially symmetric. In the case of the (001) [100] scan (A), shown in relation to the (c) ST and (d) FT polarization patterns, only L and ST waves are observed [23,24].

Every and Sachse [24] have also done scan images on (110)- and (111)-oriented Si crystals, represented by scan lines B and C respectively in Fig. 10(c) and (d). For scan image B, the FT modes are almost completely sagittally polarized, dominating the image, and there is no discernible presence of the ST modes which are almost completely SH-polarized. For scan image C, because of the conical-point polarization singularity, one half of the scan line is in the region where the ST modes are sagittal and the FT modes are SH, and the other half of the image is in the region where the FT modes are sagittal and the ST modes SH. As expected, one half of the image features only L and ST modes, and the other half only L and FT modes.

### 3.3. The degenerate features of transverse isotropy (hexagonal crystals)

The acoustic surfaces of transversely-isotropic solids and hexagonal crystals, whose linear elastic behavior conforms to transverse isotropy, have full rotational symmetry about the zonal [001] axis. One sheet of the slowness surface represents pure transverse (PT) modes and the other two sheets quasi-transverse (QT) and quasi-longitudinal (QL) modes. There is touching contact between the PT and QT sheets of the slowness surface along the zonal axis. Depending on the values of the elastic constants, the PT and QT sheets may intersect along circles, as shown in Fig. 11. Should the elastic constants satisfy the inequality

$$\frac{(C_{13} + C_{44})^2}{[C_{11}(C_{33} - C_{44})]} > 1, \tag{12}$$

the QT slowness sheet is concave in the vicinity of the zonal axis, entailing a circle of parabolic points further out on the surface where all rays point along the axis (see Fig. 11). This effect is known as external conical refraction, whereby a cone of slowness vectors all have the same ray, and whereby the circular parabolic line maps onto a single point in the wave surface. In the neighborhood of this point the wave surface is shaped as a double cone. Kim et al. [27,28] have studied the external conical refraction caustic in zinc using a variety of techniques based on piezoelectric, capillary-fracture or laser generation, and incorporating piezoelectric or capacitive detection. Fig. 12(a) shows the calculated QT focusing intensity near and along the axis, and, for comparison, Fig. 12(b) shows the QT focusing intensity measured by Kim et al. using a laser source and a longitudinal-wave piezoelectric detector.
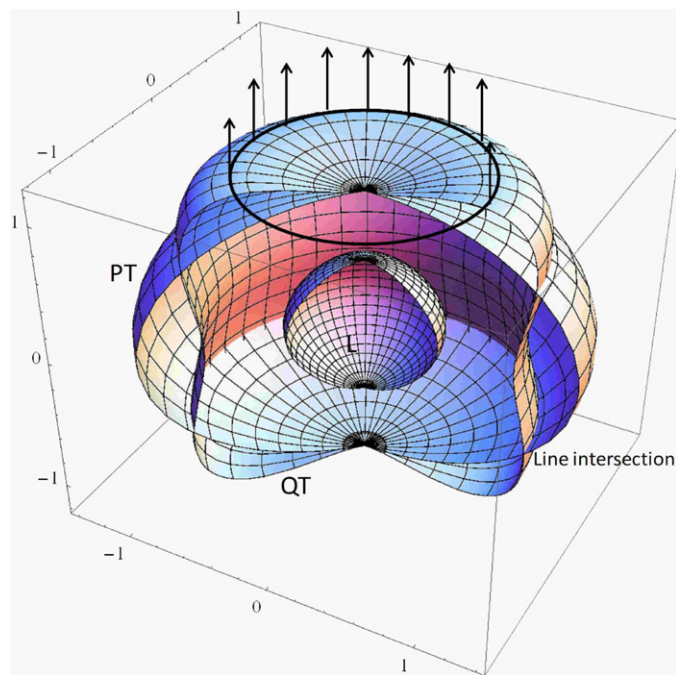
Fig. 11. Slowness surface for a transversely isotropic solid showing line intersections and external conical refraction.
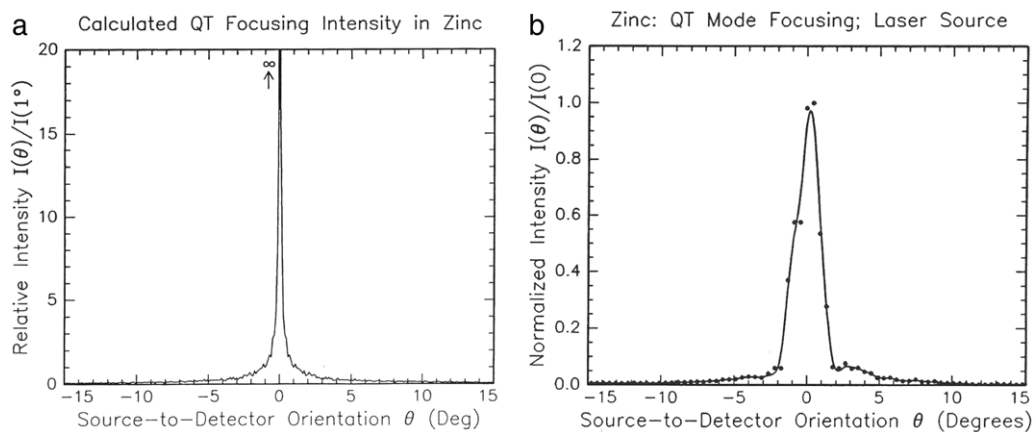

Fig. 12. (a) Calculated and (b) measured focusing in a zinc crystal [27,28].

The degenerate features discussed above are all removed when there is lowering of material symmetry, say to C_3 [29]. In that case there is no longer axial symmetry of the acoustic surfaces and no longer uncoupling of the PT from the other two slowness sheets, and the modes are appropriately classified as quasi- L, FT and ST; the intersection (line degeneracy) between the PT and QT slowness sheets is avoided, leaving only 6 points of conical degeneracy between what are now the FT and ST sheets, patched together respectively from the inner and outer portions of the PT and QT sheets. The ST sheet has narrow furrows in the region where the intersections were, and inside these furrows the Gaussian curvature is negative. The bounding parabolic lines map onto pairs of caustics, interspersed with cusps, which encircle the zonal axis. The splitting of the tangential degeneracy into a set of 4 conical points, as shown in Fig. 3, leads to a pattern of caustics with 3-fold symmetry. The lowering the symmetry from C_6 to C_3 causes the parabolic line in the slowness surface to deviate from circular, and the point external conical-refraction caustic unfolds onto a line caustic interspersed with 6 cusps. These developments are all described in detail in [29].

3.3.1. The structural stability of conical points

We have seen how tangential and line degeneracies unfold into patterns of conical points when the symmetry is lowered from C_6 or C_4, and how conical points are a generic feature of slowness surfaces and do not require material symmetry for
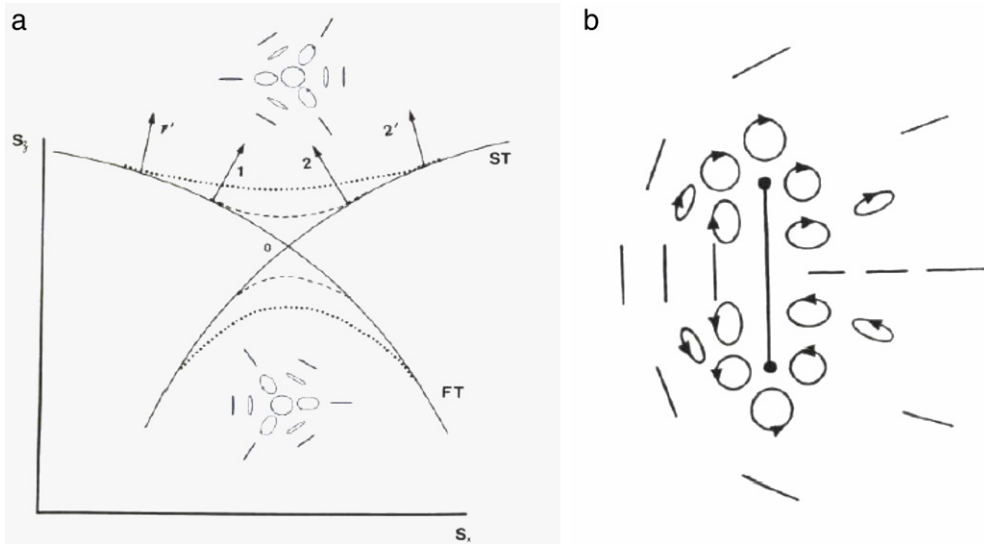
Fig. 13. (a) Splitting of a conical point through first-order spatial dispersion [32]. (b) Splitting of a conical point into two essential singularities through viscoelasticity.
Source: adapted from Shuvalov and Scott [35].

their existence. Conical points are structurally stable within the domain of ideal linear anisotropic elasticity. Outside this domain there are two recognized ways in which conical points can unfold.

First-order spatial dispersion is a phenomenon occurring in certain crystals lacking inversion symmetry [30,31]. These crystals exhibit acoustic gyrotropy, which is the splitting of the degenerate conical point modes into left- and right-circularly or elliptically-polarized modes (see Fig. 13(a)) [30–34]. The splitting, which is proportional to frequency, gives birth to initially faint caustics. Every [32] has ascribed certain features in the phonon image of quartz to this phenomenon.

Shuvalov and Scott [35] and Alshits and Lyubimov [36] have described how viscoelasticity causes splitting of a conical point, other than the one along a 3-fold axis, into a pair of essential singularities, as shown in Fig. 13(b). The slowness sheets now represent connected Riemann sheets, and in the vicinity of the singularities the modes are elliptically polarized (see Fig. 13(b)). Alshits [36] has suggested that these effects may be experimentally observable.

3.4. Intermediate- and near-field phenomena: elastodynamic Green's functions

The phonon focusing and wave-arrival effects that have been discussed in earlier sections are all far-field phenomena, in which the distance between the source and detector greatly exceeds the characteristic wavelength of the radiation, and where the ray approximation provides an adequate description. In the remainder of Section 3 we discuss measurements carried out in the near field using coherent excitation. The interpretation of these requires a consideration of diffraction integrals in the calculation of the displacement field. The nature of the experiments is such that they can be reasonably well modeled on the basis of the frequency- and time-domain elastodynamic Green's functions $G_{kp}(\mathbf{x}, \omega)$ and $G_{kp}(\mathbf{x}, t)$, respectively, for an infinite elastically anisotropic continuum.

3.4.1. Scanning transmission acoustic microscopy measurement of the frequency-domain Green's function $G_{kp}(\mathbf{x}, \omega)$

We consider here the displacement response, $G_{kp}(\mathbf{x}, \omega)$, of an infinite anisotropic solid to a time-harmonic point force. This Green's function has integral representation [37,38]

$$G_{kp}(\mathbf{x}, \omega) = \frac{1}{8\pi^2 \rho} \sum_{j=1}^{3} \left\{ \frac{1}{x} \int_0^{2\pi} d\phi\, s_j^2 \Lambda_{kp}^{\mathbf{n}j} - i\omega \int_{\cap} d\Omega\, s_j^3 \Lambda_{kp}^{\mathbf{n}j} \exp\left(i\omega \mathbf{s}_j.\mathbf{x}\right) \right\}, \tag{13}$$

the integrations being with respect to the direction of the wave normal $\mathbf{n}$. The sum is over the three acoustic branches j, and $\Lambda_{kp}^{\mathbf{n}j} = U_k^j U_p^j$, where $\mathbf{U}^j(\mathbf{n})$ is the branch polarization. The second integral is over the forward hemisphere centered on the observation direction, and the first integral is over the periphery of this hemisphere.

Scanning transmission acoustic microscopy (TAM) has been used by Hauser et al. [39,40] to study the response of a number of anisotropic solids, including metal, insulating and semi-conducting crystals and fiber composites, to time-harmonic point-like excitation. Grill et al. [40–43] have used essentially the same technique to study a number of crystals, with the difference that they also retain phase information and operate at higher frequencies. The experimental setup is shown in Fig. 14. A pair of water-immersion acoustic lenses, which are focused to small spots on opposite surfaces of the
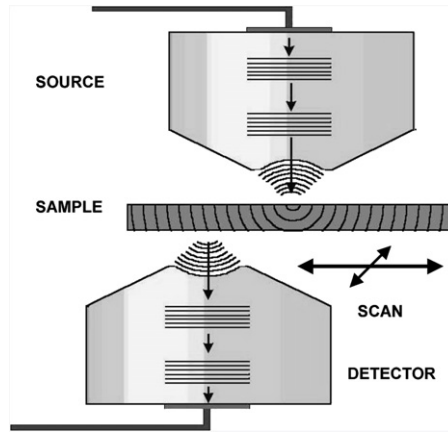
Fig. 14. Schematic representation of the transmission-acoustic-microscopy setup for measuring G_{33} ($\mathbf{x}$, ω) [41].

sample, are used to generate and detect ultrasonic tone bursts. One of the transducers is kept fixed while the other is raster scanned to yield a 2D image of the ultrasonic flux pattern transmitted through the sample. The measured diffraction images are in good agreement with Green's functions $G_{33}(\mathbf{x}, \omega)$ calculated from experimental parameters.

Fig. 15 shows calculated and measured results for [100]-oriented GaAs and Si single crystals. Because the excitation and detection is axisymmetric, the SH-polarized FT modes do not feature in these images, and time gating has been used to remove the L modes. Fig. 15(a) shows the focusing pattern that one would expect to observe in the far field, where diffraction fringes are too fine to be resolved. This is a focusing pattern like those discussed earlier. Emerging from the far field, as the frequency is lowered or the observation point is brought closer to the source, the line and cusp caustics unfold into Airy and Pearcey diffraction patterns respectively [20,44]. As the frequency is lowered further, the fringes broaden and merge, becoming progressively fewer in number [45]. To predict the diffraction pattern requires going beyond the stationary phase approximation and carrying out the numerical integration in Eq. (13). Fig. 15(b) shows a measured TAM-amplitude image for of a 4.8 mm thick, (100)-oriented GaAs crystal for $f = 362$ MHz, and Fig. 15(c) shows the corresponding calculated image based on optimized elastic constants [43]. Fig. 15(d) shows a measured amplitude image for Si(001) for $d = 2$ cm, and $f = 15$ MHz [40]. Fig. 15(e) shows the corresponding calculated phase image for $f = 10$ MHz, the smooth variation in shading from white to black representing a phase variation from 0 to 2π, and the discontinuous jumps back to white being where the phase wraps around back to zero. In evidence in Fig. 15(e) are a number of phase singularities or acoustic vortices, in a small circuit around which the phase changes by $\pm 2\pi$.

3.4.2. Measurement of time-domain Green's function $G_{kp}(\mathbf{x}, t)$: capillary-fracture-generated waveforms

We consider here the measurement of the displacement response $G_{kp}(\mathbf{x}, t)$ of an infinite anisotropic solid to a suddenly applied point force. This Green's function has integral representation [46,47]

$$G_{kp}(\mathbf{x}, t) = \frac{\Theta(t)}{8\pi^2 \rho} \sum_{j=1}^{3} \left\{ \frac{1}{x} \int_0^{2\pi} d\phi s_j^2 \Lambda_{kp}^{\mathbf{n}j} - \int_{\cap} d\Omega s_j^3 \Lambda_{kp}^{\mathbf{n}j} \delta\left(t - \mathbf{s}_j.\mathbf{x}\right) \right\}. \tag{14}$$

The first term is the static Green's function and the second term determines the time dependence. Integration over direction is done numerically in the example below.
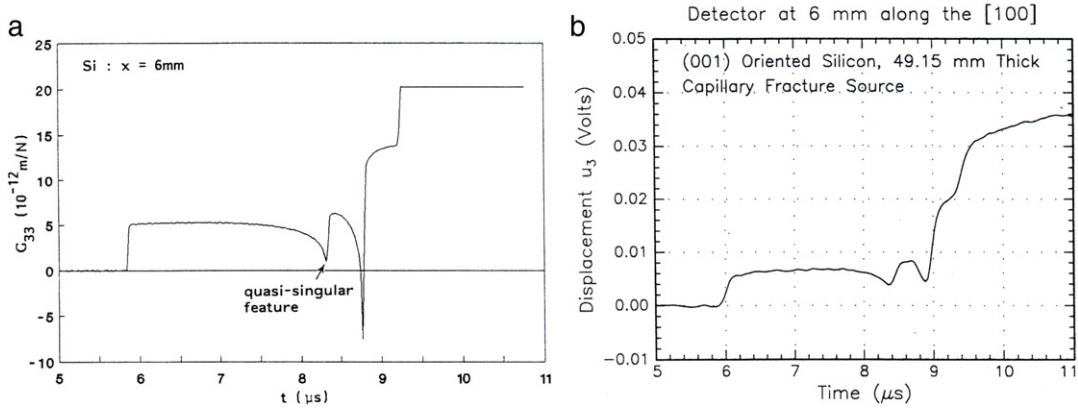
Fig. 16(a) shows a calculated Green's function $G_{kp}(\mathbf{x}, t)$ for silicon, with force and displacement in the $k = p = 3$ cube direction and $\mathbf{x} = (6.0, 0, 49.15)$ mm [46]. Fig. 16(b) shows the measured displacement response of an (001)-oriented silicon crystal of thickness 49.15 mm to a sudden force applied to one surface [46]. This figure also shows the displacement measured at 6 mm from epicenter in the [100]-direction on the opposite surface. The force is generated by the fracturing of a very fine capillary caused by slowly increasing the pressure applied to it by a razor blade. At the moment fracture occurs, the localized pressure that the capillary was exerting on the surface is removed. The displacement is measured by a small capacitive transducer mounted on the surface, which yields a voltage output replicating rather closely the surface displacement [48].

The calculated and measured displacement responses are not strictly equivalent, since the former applies to an infinite continuum and the latter to a plate with free surfaces. Nevertheless, because the measurements are done near to epicenter, and the time window captures only the first direct bulk-wave arrivals, the calculated and measured responses are comparable. In particular, the wave arrivals – the sharp features in Fig. 16(a) – have the same analytical forms and arrival times a infinite continuum and half-space calculations.
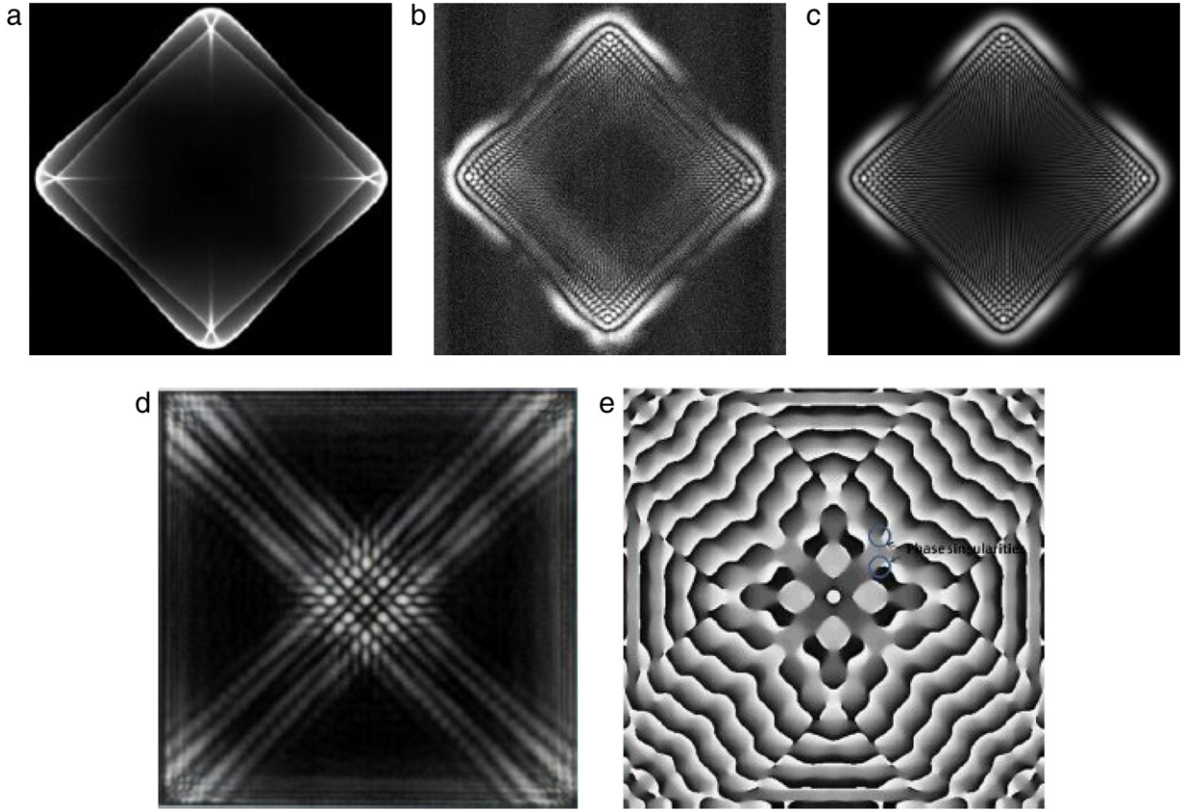
Fig. 15. (a) Focusing pattern for GaAs (001). (b) Measured and (c) calculated TAM amplitude images for a 4.8-mm thick, (100)-oriented GaAs crystal for $f = 362$ MHz and using optimized elastic constants [43]. (d) Measured amplitude image for a (100)-oriented 2-cm Si cube at 15 MHz [40]. (e) Calculated phase images for Si (001) for a (100)-oriented 2-cm Si cube at 10 MHz.

Fig. 16. (a) Calculated, and (b) measured displacement response (Green's) functions for silicon [46].

3.4.3. Wave arrival singularities in $G_{kp}(\mathbf{x}, t)$

$G_{kp}(\mathbf{x}, t)$ is dominated by sharp features arising from integration over points on the slowness surface where the outward normal or ray vector is parallel to $\mathbf{x}$ and where $\mathbf{s}_j.\mathbf{x}$ is stationary. These singularities propagate outwards from the source at the group velocity $\mathbf{V}$, and are known as wave arrivals. In the discussion below the indices k, p are suppressed for simplicity [46]. The stationary phase approximation is invoked, integrating over a small region of slowness surface around $\mathbf{s}_0$ approximated for a generic point on the slowness surface by $s_3 = - \left(\alpha s_1^2 + \beta s_2^2 \right)$ in local coordinate system, with s_3 normal to the surface and 2α and 2β being the principal curvatures of the slowness surface. Substituting $d\Omega = ds_1 ds_2 \cos\psi / s_0^2 =$

$ds_1 ds_2/(V_0 s_0^3)$, $F = \Lambda/8\pi^2 \rho V$ and $t - \mathbf{s}.\mathbf{x} = t - \mathbf{s_0}.\mathbf{x} + s_3 x = T + \left(\alpha s_1^2 + \beta s_2^2\right) x$ for $T = t - |\mathbf{x}| / |\mathbf{V}_0|$, we have

$$G(x, t) = -F \int ds_1 ds_2 \delta \left(T + \left(\alpha s_1^2 + \beta s_2^2\right) x \right), \tag{15}$$

and on integrating one obtains

$$G(x, t) = \frac{-F}{\sqrt{|\alpha\beta|} x} \begin{cases} \pi \Theta(-T); & \alpha, \beta > 0 \\ \pi \Theta(T); & \alpha, \beta < 0 \\ \ln(T); & \alpha\beta < 0. \end{cases} \tag{16}$$

Thus, we see that for convex and concave portions of the slowness surface, the associated wave arrivals are in the form of discontinuities, whereas for saddle-shaped portions a logarithmic singularity ensues. In both cases there is a leading factor $1/\sqrt{|\alpha\beta|} = 4/\sqrt{|K|}$ in the displacement amplitude, and hence the energy propagated by the wave arrival, which is proportional to the square of the displacement, is inversely proportional to the Gaussian curvature K as deduced from the ray approximation. Where one of the principal curvatures goes to zero, the energy flux diverges on a caustic and a higher order expansion for the equation of the slowness surface is required to determine the response [46].

4. Surface acoustic wave phenomena; surface Green's function $\mathrm{Im}G_{33}(\mathbf{k}_\parallel, \omega)$

A useful vehicle for revealing the full richness of the surface dynamics of both isotropic and anisotropic solids is the Fourier-domain surface dynamic Green's function $G_{ij}(\mathbf{k}_\parallel, \omega)$. This function represents the ith component of the displacement response of a surface to a distributed force acting on the surface in the x_j direction, the temporal and surface spatial frequencies of which are ω and $k_\parallel = (k_1, k_2)$, respectively [49–51].

For a force acting in the x_j direction on the otherwise free surface of a solid occupying the domain $x_3 > 0$, the displacement field $\mathbf{u}$ in the solid is required to satisfy the wave equation (Eq. (1)) and the boundary conditions:

$$\sigma_{l3}(\mathbf{k}_\parallel, \omega; x_3 = 0_+) = -\delta_{lj}. \tag{17}$$

The displacement field takes the form of a linear superposition of three phase-matched outgoing homogeneous or evanescent partial waves:

$$u_i^{(j)}(\mathbf{k}_\parallel, \omega; x_3) = \sum_{n=1}^3 A_j^{(n)} U_i^{(n)} \exp(i k_3^{(n)} x_3). \tag{18}$$

From the stress–strain relationship and the boundary conditions, the three partial wave amplitudes $A_j^{(n)}$ are governed by a set of linear equations, having solution

$$A_j^{(n)} = \frac{i}{\omega} (\mathbf{B}^{-1})_j^{(n)} = \frac{i}{\omega} \frac{adj(\mathbf{B})_j^{(n)}}{\det |\mathbf{B}|}; \quad B_l^{(n)} = c_{3lpq} U_p^{(n)} s_q^{(n)}. \tag{19}$$

The surface Green's function for force and displacement-response normal to the surface is obtained by taking the limit $x_3 \to 0_+$ and setting $ij = 33$:

$$G_{33}(\mathbf{k}_\parallel, \omega) = \frac{i}{\omega} \sum_{n=1}^3 \frac{adj(\mathbf{B})_3^{(n)} U_3^{(n)}}{\det |\mathbf{B}|}. \tag{20}$$

Fig. 17(a) shows $G_{33}(\mathbf{k}_\parallel/\omega)$ as a function of $\mathbf{s}_\parallel = \mathbf{k}_\parallel/\omega$ at fixed frequency for the [100] direction in the (001) surface of the cubic crystal copper. The imaginary part $\mathrm{Im}G_{33}(\mathbf{k}_\parallel/\omega)$ has kinks at the limiting L (a), FT (b) and ST (c) slownesses (lateral waves), and is zero after the ST threshold (c) (transonic state), except at the Rayleigh wave slowness (RW) where it has a sharp spike associated with the pole of $G_{33}(\mathbf{k}_\parallel/\omega)$, which is determined by the vanishing of the boundary condition determinant $\det |\mathbf{B}|$ [52,53]. Some attenuation has been introduced to broaden the Rayleigh peak from a delta function and render it visible in the diagram.

Fig. 17(b) shows $\mathrm{Im}G_{33}(k_\parallel/\omega)$ represented by a gray scale as a function of $s_1 = k_1/\omega$ and $s_2 = k_2/\omega$ at fixed frequency for the (001) surface of copper. Because of the 4-fold symmetry axis normal to the surface, the pattern repeats itself in the other three quadrants. Here we can see how the lateral waves vary with direction, undergoing splitting in some directions. The Rayleigh wave shows considerable variation with direction, both in slowness and in intensity. Towards the [110] direction the polarization of the RW tilts over towards the horizontal, and it becomes more weakly coupled to G_{33}, and hence the RW decreases in intensity, ultimately vanishing as it degenerates with the limiting T bulk wave in the [110] direction. Also, as the RW approaches this degenerate condition, its displacement field penetrates ever more deeply into the solid, which also makes it more weakly coupled to any component of the surface response. Extending out about 20° on either side of the [110] direction is a sharp resonance in the bulk-wave continuum associated with a pseudo-surface wave (pSAW). This is a wave consisting predominantly of two evanescent partial waves, but in addition there is a small bulk wave component which radiates the energy of this wave away from the surface, causing its attenuation. For the pSAW the boundary condition determinant is very small but non-zero, except in isolated directions where the pSAW becomes a true supersonic surface wave [54].
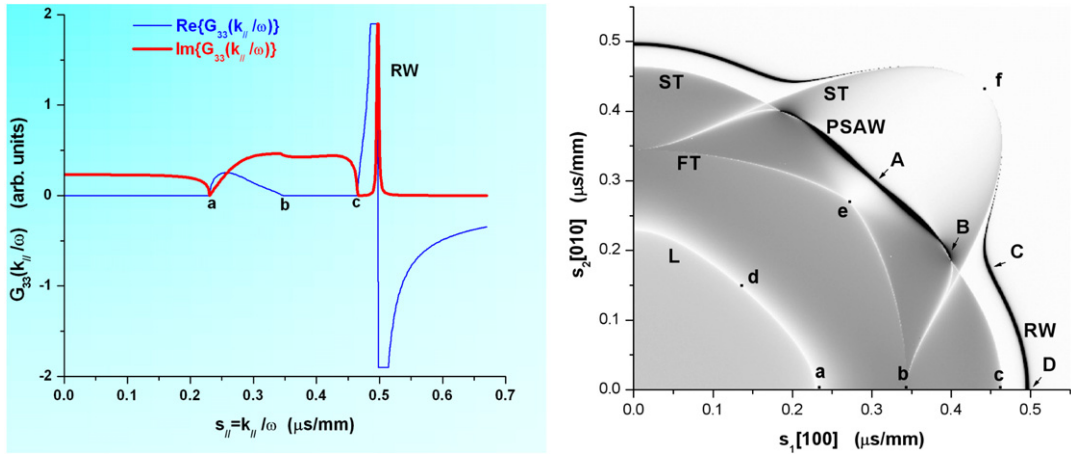
Fig. 17. (a) $G_{33}(k_\parallel/\omega)$ for [100] direction in Cu(001), and (b) gray scale representation of $\mathrm{Im}G_{33}(k_\parallel/\omega)$ for $\mathbf{s}_\parallel = k_\parallel/\omega$ in Cu(001).
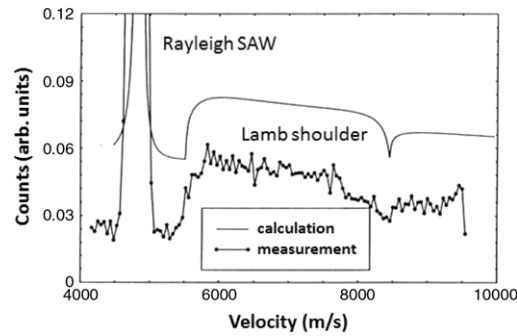
Fig. 18. Measured and calculated SBS spectra of $VC_{0.75}$ for the $[1\bar{1}0]$ direction in the (110) surface [57].

### 4.1. Surface Brillouin scattering

Surface Brillouin scattering (SBS) is an experimental technique that gives direct access to the imaginary part of the surface Green's function [55,56]. A laser beam of frequency ω_0 and wave number $k = \omega_0/c$ is incident on the highly polished surface of a sample at an angle θ to the surface normal, and the back-scattered light, shifted in frequency by ω, is collected and analyzed. For an opaque solid the frequency shift is caused by dynamic fluctuations of the wave vector $k_\parallel = 2k\sin\theta$ in the surface profile resulting from the thermal equilibrium distribution of bulk and surface phonons having wave vector component $k_\parallel$ at the surface. Through the fluctuation–dissipation theorem it follows that the scattering cross section is given by [55,56]

$$\frac{d^2\sigma}{d\Omega d\omega} = \frac{AT}{\omega}\mathrm{Im}G_{33}\left(k_\parallel, \omega\right), \tag{21}$$

where A is a constant that depends on the scattering geometry and the frequency and polarization of the light. Comparison of a measured and calculated SBS spectrum for vanadium carbide ($VC_{0.75}$) is shown in Fig. 18 [57].

An extensive literature exists on SBS, and the technique is regularly used for determining the near-surface elastic properties of solids. In many of these studies the angular dependences of the SAW and pSAW velocities have been measured, and in some [58] the angular variation of the pSAW intensity has also been measured and a minimum at the secluded supersonic SAW commented on.

SBS is a valuable tool in the determination of the elastic properties of thin near-opaque sub-micron supported films that critically depend on the synthesis conditions. With the SBS frequency being in the range 1–50 GHz, and the wave field penetrating to about a wavelength below the surface, this technique is very suitable for studying such films. The evaluation of $\mathrm{Im}G_{33}(\mathbf{k}_\parallel/\omega)$, used in the interpretation, takes into account also the 6 phase-matched partial waves in the film, and also the 6 additional boundary conditions of continuity of displacement field and traction force at the interface. The velocity dispersion curves of the surface excitations are measured as a function of $k_\parallel d$, where d is the film thickness, and appropriate fitting routines are used to extract the material constants. As an illustration, stoichiometric, homogeneous WC films were grown using RF (radio-frequency) sputtering with steps of differing thickness (60–655 nm) on a silicon substrate by Wittkowski et al. [59]. With the high mass density of WC, the system falls into the "slow film on fast substrate" category, yielding the
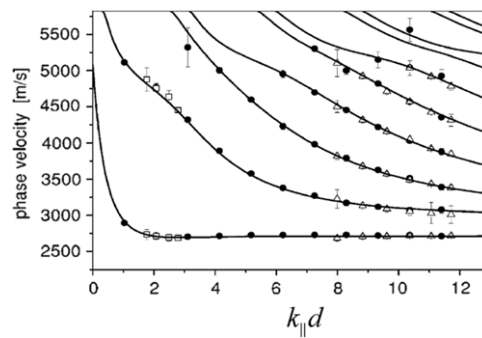
Fig. 19. Phase velocity dispersion curves for WC films on a silicon substrate, calculated using optimized values of elastic constants and density for the film. Measured data for various film thicknesses and scattering angles is shown by the symbols [59]. The lowest branch represents the Rayleigh wave and the higher branches the various orders of Sezawa modes.

Rayleigh SAW and many Sezawa modes. Fig. 19 shows the measured data and calculated phase velocity dispersion curves that have been obtained by adjusting the elastic constants and density of the film to obtain a best fit.

4.2. Reflection and "birefringence" of SAW

Many of the characteristics of bulk waves are shared by surface waves, but with reduction of dimensionality from 3 to 2. Thus, corresponding to the 3D slowness surfaces of bulk waves there are the 2D slowness curves (which, for convenience, we term surfaces) of SAW and pSAW. In the far field we observe distributions of rays, which are normal to the slowness surface, and which define the ray surface. In 3D, one of the important uses of the slowness surface is in treating reflection and transmission at plane surfaces and interfaces. Incident and outgoing waves must all phase match in the interface, and this requires that they all be of the same frequency ω and have the same component of slowness $\mathbf{k}_\parallel$ in the interface. The normal component of slowness must satisfy the slowness equation, i.e. be a point on the slowness surface which corresponds to an outgoing wave. There are between one and three outgoing rays in each medium, the remaining solutions corresponding to evanescent waves.

Every and Maznev [60] have demonstrated that the same line of reasoning applies to reflection of SAW at a straight edge. Fig. 20 shows the results of an experiment in which a line-focused laser pulse generates a SAW beam on the (111) surface of a GaAs crystal. The surface is covered with a thin layer of fine alumina particles, and the acceleration of the surface by the SAW shakes off the alumina particles and renders the SAW path visible. On incidence on the edge of the crystal the SAW's energy is split between scattered bulk waves, which recede from the surface and out of view, and reflected SAW and pSAW. The ray splitting is clearly visible in Fig. 20(a), and the interpretation in terms of the slowness surface and rays is provided in Fig. 20(b) and (c). Whilst in 3D the number of outgoing homogeneous waves in each medium is a maximum of 3, it is not known at this stage what the maximum number of SAW and pSAW is [60].

4.3. Phonon focusing of SAW

The far-field radiation pattern for a point source of SAW and pSAW on an anisotropic solid tends to be highly non-uniform because it depends inversely on the curvature of the slowness surface. Points of zero curvature in the slowness surface map onto caustics in the surface-wave energy flux. This has been demonstrated very clearly in a series of experiments by Kolomenskii and Maznev [61–63] using a point-focused laser pulse for the excitation of SAW and the powder technique to observe the directions of most intense SAW radiation. Fig. 21(a) shows results for GaAs (111), and Fig. 21(b) shows their interpretation. The slowness surface has 6 alternating concave and convex regions, giving rise to 6 folded regions, each bounded by a pair of cusps, in the wave surface. Each of these cusps generates a caustic in the intensity field. The possible SAW focusing patterns on cubic crystals have been surveyed by Maznev and Every [64].

Phonon focusing is also exhibited by the guided modes of anisotropic plates [65]. The recent spike of interest in plate-mode focusing [66–69] is related to practical needs of ultrasonic non-destructive testing of fiber-reinforced composite plates. In the long wavelength limit, composite materials are described by an elastic stiffness tensor similar to that of crystals, and often they possesses strong elastic anisotropy. Focusing of guided plate modes is influenced by wave dispersion [66,67], which makes it a richer phenomenon compared to the focusing of SAWs on semi-infinite surfaces.
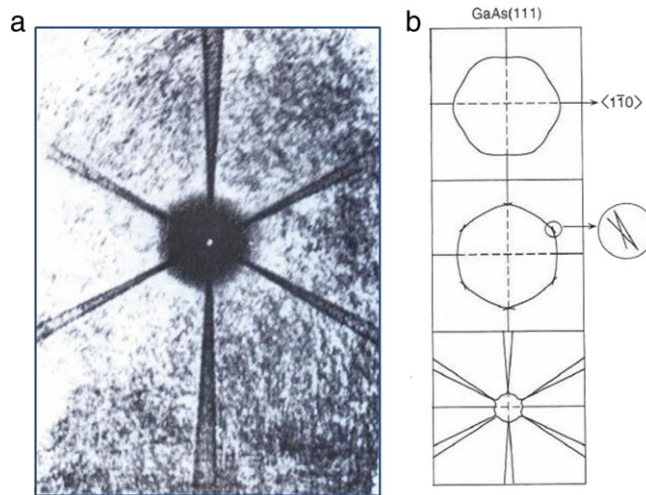
4.4. Space–time domain surface Green's function $G_{33}(\mathbf{x}, t)$

Fig. 22 shows the calculated and measured surface Green's function $G_{33}(\mathbf{x}, t)$ for a (001)-oriented copper single crystal [70,71]. Capillary fracture has been used to simulate a suddenly-applied point force, and a capacitive detector has been used to measure the displacement response elsewhere on the same surface. The response is dominated by the sharp
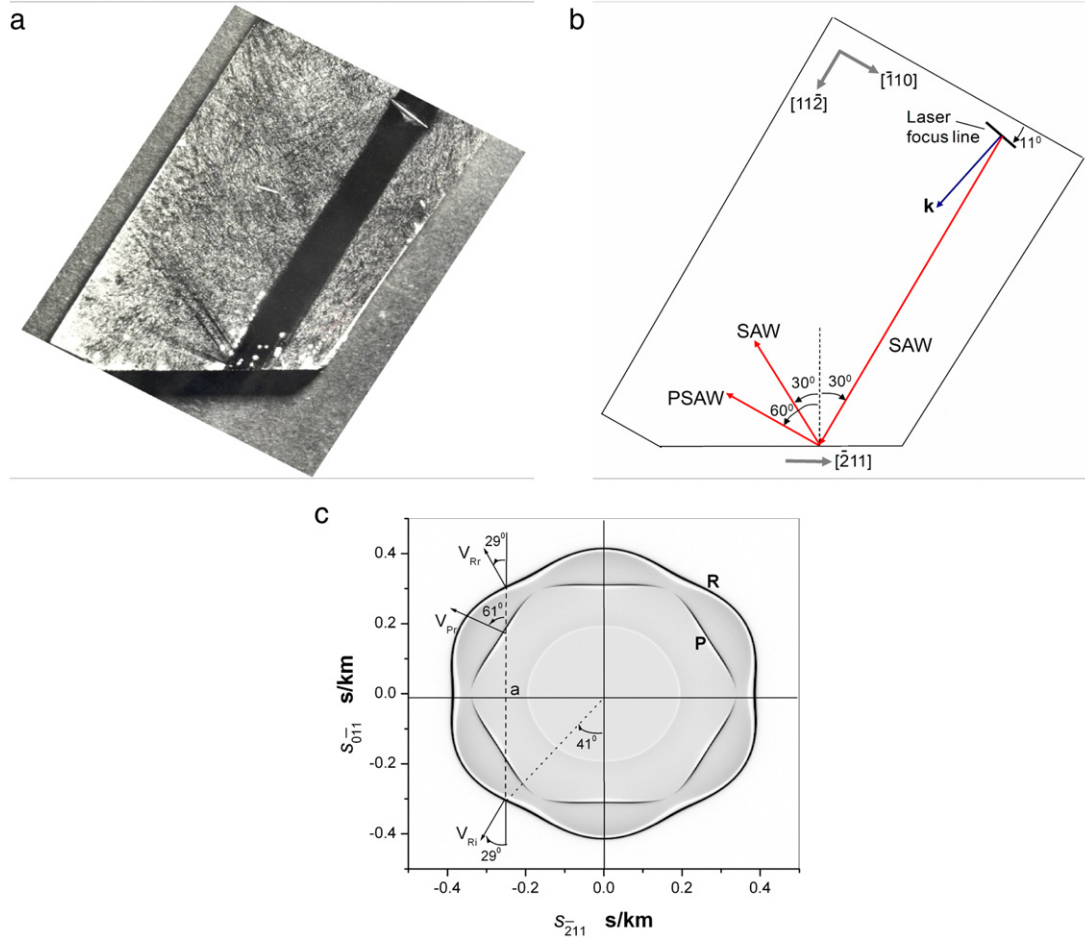
Fig. 20. Ray splitting in the reflection of a SAW at the edge of a (111)-oriented GaAs crystal [60]. (a) Observed SAW trace, (b) ray diagram, and (c) slowness surface interpretation, R denoting the SAW (Rayleigh wave) slowness and P the pSAW slowness.

Fig. 21. (a) Observed focusing pattern for laser-generated SAW on GaAs(111). (b) From top, calculated SAW slowness surface, wave surface, and focusing pattern for GaAs (111) [61,63].

SAW wave arrivals d, e and f, and there are also the lateral wave arrivals a, b and c. Because of the folding of the SAW wave surface, in the [100] direction there are 3 distinct SAW arrivals (and in adjacent directions there are five distinct arrivals,
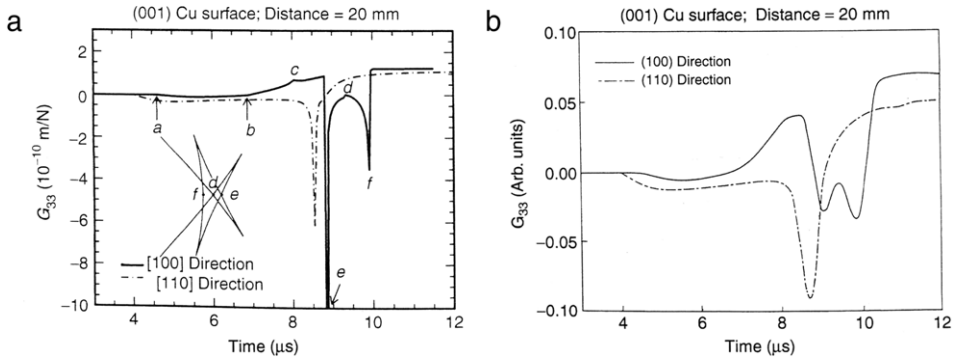
Fig. 22. (a) Calculated and (b) measured surface Green's function $G_{33}(\mathbf{x}, t)$ for a (001)-oriented copper single crystal [70,71].

two pairs becoming coincident in the [100] direction). Note that arrival f is "normal" in the sense that it is preceded by a negative divergence and terminated with a discontinuity, whereas for arrival e this sequence is reversed. The reason for the behavior of the latter is that wave arrival e is associated with a concave region of the SAW slowness surface. Bearing in mind the rounding of the experimental data, there is reasonable agreement between the calculated and measured responses.

4.5. Observation of SAW wave front propagation

The propagation of 100 MHz–1 GHz SAW on crystals can be visualized in the temporal domain using an ultrafast optical method [72,73]: tightly-focused, periodic pump light pulses of sub-picosecond duration are focused onto a point on a bare or metal-coated crystal surface to generate the SAW. Similarly focused ultrashort probe light pulses are scanned over the surface and interferometrically detected to form images at different delay times with respect to the pump pulses. The typical imaging area covers a few 100 μm in linear x and y scans, and the lateral spatial resolution is about 1 μm. Typical surface displacements are about 0.01 nm. The acoustic field imaged is the out-of-plane surface particle velocity. The wave front patterns in the case of minimal structural wave dispersion represent the group velocity contours of the crystal surface.

Fig. 23(a) shows such a 135×135 μm^2 acoustic-field image of a TeO$_2$ (001) surface covered with a 40-nm thickness gold film (the latter allowing optical absorption without significantly introducing structural wave dispersion). TeO$_2$ is a tetragonal crystal with an extremely high anisotropy [74]. The excitation light is focused at the center of the image, which is recorded at a time 8.0 ns after the arrival of the pump light pulse. Different acoustic modes are clearly distinguished, as well as multiple wave fronts for each mode because of the periodic laser excitation with a 12.5-ns repetition period. Fig. 23(b) shows a finite-difference time-domain (FDTD) simulation of the surface velocity normal to the surface for the bare crystal surface. The features in Fig. 23(a) are reproduced well. Fig. 23(c) shows the corresponding calculated group velocity contours using standard elasticity theory: the blue, red and green lines represent, respectively, SAW, pSAW and L bulk waves. The pSAW are intrinsically lossy, even in the absence of material attenuation, although this effect is not marked compared to geometrical attenuation (caused by the expanding wave fronts). Some modes with shear polarization are missing in Fig. 23(a) and (b) because of their lack of surface-normal displacement components [74]. Such modes can in fact be imaged using a related ultrafast photoelastic imaging technique sensitive to in-plane shear strain [75].

Time-resolved imaging involves acoustic-field data in the form $f(\mathbf{r}, t)$, were $\mathbf{r}$ is the two-dimensional position vector. In the ideal case, the spatiotemporal Fourier transform of $f(\mathbf{r}, t)$,

$$F(\mathbf{k}, \omega) = \frac{1}{(2\pi)^3} \int d^2\mathbf{r}\, dt\, f(\mathbf{r}, t)\, e^{-(\mathbf{k}\cdot\mathbf{r}-\omega t)},$$

takes a finite value only if $(\mathbf{k}, \omega)$ satisfies the dispersion relation $\omega = \omega(\mathbf{k})$ of the possible acoustic modes with in-plane wave vector $\mathbf{k}$ [76]. The experimental contours represented by $|F(\mathbf{k}, \omega)|$, plotted in $\mathbf{k}$-space at constant angular frequency ω, are therefore useful to understand the crystal dispersion. The equivalent plot in $\mathbf{k}/\omega$ space is the slowness curve, which is frequency independent provided that the k vs. ω dispersion curve is linear for any $\mathbf{k}$ (as is the case here). Fig. 24(a) shows a plot of the Fourier amplitude $|F(\mathbf{k}, \omega)|$ in $\mathbf{k}$-space at 570 MHz, which follows the slowness curve for TeO$_2$ (001). These results agree very well with the theoretical calculation shown in Fig. 24(b), where the colors represent each mode as in Fig. 23(c). Thus time-resolved imaging experiments can be used for direct observation of complicated dispersion relations for various acoustic modes in crystals. This method has also been used to image surface acoustic waves travelling from grain to grain in single-crystal copper [77].

5. Discussion and conclusions

The purpose of this paper has been to provide a broad overview of the experimental methods of crystal acoustics and the results emerging, and to explain the observations in terms of the acoustic slowness and wave surfaces of anisotropic solids,
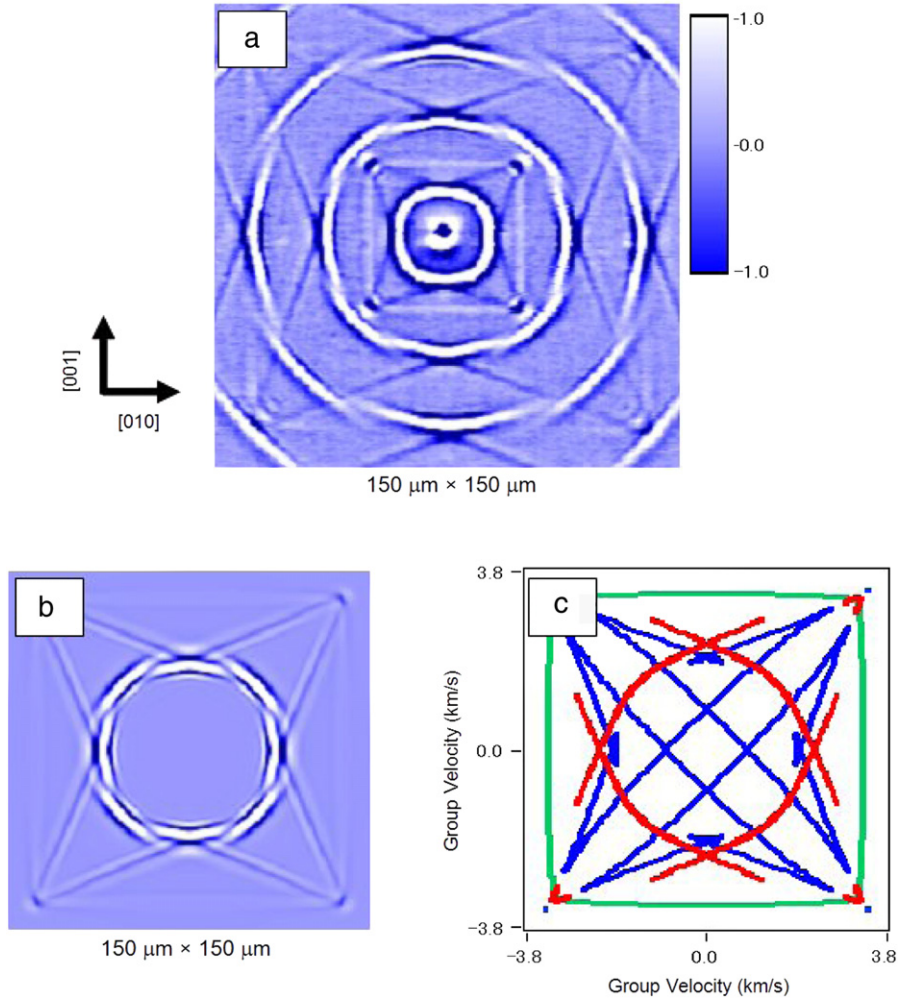
Fig. 23. (a) A snapshot of the velocity of the surface-normal motion on a TeO$_2$ (001) surface recorded 8 ns after optical excitation at the center. The imaged area is 150 × 150 μm^2 (b) FDTD image of the velocity of surface-normal motion. (c) Mode calculation for the TeO$_2$ (001) surface. Blue curves: surface acoustic waves. Red curves: pseudo-surface waves. Green curves: longitudinal bulk waves. (For interpretation of the references to colour in this figure legend, the reader is referred to the web version of this article.)
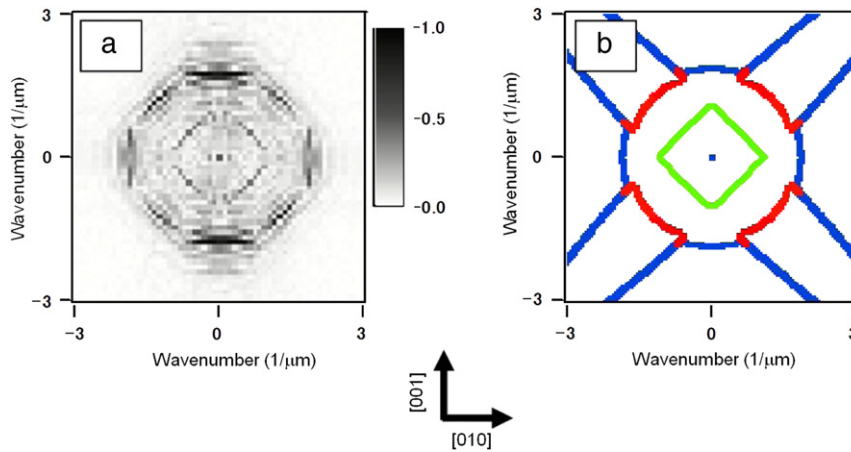
Fig. 24. (a) Spatiotemporal Fourier amplitude F (**k**, ω) obtained from the experimental results for a TeO$_2$ (001) surface. (b) Theoretical calculation for the constant-frequency contours (effectively slowness curves). Colors are the same as Fig. 23(c). (For interpretation of the references to colour in this figure legend, the reader is referred to the web version of this article.)

and the special features they possess. It is interesting to observe that multiple connections exist between this classical field and some areas of physics that have attracted considerable attention in the last decade. There is for example the recently discovered phenomenon of self-collimation, i.e. diffractionless propagation of light in certain directions in photonic crystals [78–80]. This effect has also been observed in acoustic wave propagation in sonic crystals [81] and years earlier for SAW on a natural crystal [82]. Self-collimation occurs in the directions of zero curvature of the slowness surface [80] and thus is closely related to phonon focusing. Another phenomenon that has attracted intense attention is negative refraction of light and sound in metamaterials [83,84]. In crystal acoustics this phenomenon is also well known [85], and is, again, related to the shape of the slowness surface. Similarly to the metamaterials case, this effect makes it possible for a planar interface to act as a "lens" yielding an image of a point source [85,86] (albeit in crystal acoustics such imaging is not aberration-free).

Unfortunately it has not been possible to cover the above-mentioned issues in any depth; it has been necessary to restrict the scope of this article to bulk waves, surface waves on plane surfaces, and waves on supported layers. There have been numerous other elegant investigations that space constraints have not allowed us to discuss, including nonlinear waves [87], wedge waves [88], meandering waves on a spherical crystal surface [89] and so on. However, we believe that the material we have covered provides ample justification for Vladimir Alshits' assertion regarding the beautiful phenomena of crystal acoustics.

Acknowledgments

References

[1] V.I. Alshits, The role of anisotropy in crystal acoustics, Sov. Phys. Acoust. 38 (1992) 614–615.
[2] B.A. Auld, Acoustic Fields and Waves in Solids, Krieger, Malabar, 1990.
[3] F.I. Fedorov, Theory of Elastic Waves in Crystals, Plenum, NY, 1968.
[4] M.J.P. Musgrave, Crystal Acoustics, Holden-Day, San Francisco, 1970.
[5] A.L. Shuvalov, Topological features of the polarization fields of plane acoustic waves in anisotropic media, Proc. Roy. Soc. Lond. A454 (1998) 2911–2947.
[6] V.I. Alshits, J. Lothe, Acoustic axes in trigonal crystals, Wave Motion 43 (2006) 177–192.
[7] A.N. Norris, Acoustic axes in elasticity, Wave Motion 40 (2004) 315–328.
[8] V.I. Alshits, A.L. Shuvalov, Polarization fields of elastic waves near the acoustic axes, Sov. Phys. Crystallogr. 29 (4) (1984) 373–378.
[9] V.I. Alshits, A.V. Sarychev, A.L. Shuvalov, Classification of degeneracies and analysis of their stability in the theory of elastic waves in crystals, Sov. Phys. JETP 62 (1985) 531–539.
[10] V.I. Alshits, A.L. Shuvalov, Acoustic axes in piezoelectric crystals, Sov. Phys. Crystallogr. 33 (1) (1984) 1–4.
[11] V.I. Alshits, The role of anisotropy in acoustics of crystals, in: Proceedings of WCU 2003, Paris, 2003, pp. 999–1006.
[12] A.G. Every, A.K. McCurdy, Phonon focusing in piezoelectric crystals, Phys. Rev. B36 (1987) 1432–1447.
[13] R. Burridge, Singularity on plane lids of wave surface of elastic media with cubic symmetry, Q. J. Mech. Appl. Math. 20 (1967) 41.
[14] A.N. Norris, Wavefront singularities associated with the conical point in elastic solids with cubic symmetry, Wave Motion 44 (2007) 513–527.
[15] H.J. Maris, Enhancement of heat pulses in crystals due to elastic anisotropy, J. Acoust. Soc. Am. 50 (1971) 812.
[16] H.J. Maris, in: W. Eisenmenger, A.A. Kaplyanskii (Eds.), Nonequilibrium Phonons in Nonmetallic Crystals, North Holland, Amsterdam, 1986.
[17] A.G. Every, Ballistic phonons and the shape of the ray surface in cubic crystals, Phys. Rev. B24 (1981) 3456–3467.
[18] G.A. Northrop, J.P. Wolfe, Ballistic phonon imaging in germanium, Phys. Rev. B22 (1980) 6196–6212.
[19] J.P. Wolfe, Imaging Phonons, Cambridge University Press, Cambridge, 1998.
[20] M.V. Berry, Waves and Thom's theorem, Adv. Phys. 25 (1976) 1–26.
[21] A.L. Shuvalov, A.G. Every, Shape of the acoustic slowness surface of anisotropic solids near points of conical degeneracy, J. Acoust. Soc. Am. 101 (1997) 2381–2383.
[22] D.C. Hurley, J.P Wolfe, Phonon focusing in cubic crystals, Phys. Rev. B32 (1985) 2568.
[23] A.G. Every, W. Sachse, K.Y. Kim, M.O. Thompson, Phonon focusing and mode conversion effects in silicon at ultrasonic frequencies, Phys. Rev. Lett. 65 (1990) 1446–1449.
[24] A.G. Every, W. Sachse, Imaging of laser-generated ultrasonic waves in silicon, Phys. Rev. B44 (1991) 6689–6699.
[25] F.V. Bunkin, A.A. Kolomenskii, V.G. Mikhalevich, Lasers in Acoustics, Harwood, Chur, 1991.
[26] V.E. Gusev, A.A. Karabutov, Laser Optoacoustics, American Institute of Physics, 1993.
[27] K.Y. Kim, W. Sachse, A.G. Every, Focusing of acoustic energy at the conical point in zinc, Phys. Rev. Lett. 70 (1993) 3443–3446.
[28] K.Y. Kim, W. Sachse, A.G. Every, Focusing of quasi-transverse modes in zinc at ultrasonic frequencies, Int. J. Mod. Phys. B8 (1994) 2327–2352.
[29] A.G. Every, Formation of phonon-focusing caustics in crystals, Phys. Rev. B34 (1986) 2852–2862.
[30] D.L. Portigal, E. Burstein, Acoustical activity and other first order spatial dispersion effects in crystals, Phys. Rev. 170 (1968) 673.
[31] A.S. Pine, Linear wave-vector dispersion of shear-wave phase velocity in alpha quartz, J. Acoust. Soc. Am. 49 (1971) 1026.
[32] A.G. Every, Effects of first-order spatial dispersion on phonon focusing: application to quartz, Phys. Rev. B36 (1987) 1448–1456.
[33] A.L. Shuvalov, On the effect of spatial dispersion on the degeneracies of acoustic wave branches in crystals, J. Acoust. Soc. Am. 104 (1998) 2008–2014.
[34] A.L. Shuvalov, A.G. Every, Evolution of phonon-focusing caustics under linear spatial dispersion, J. Phys. A: Math. Gen. 33 (2000) 5105–5116.
[35] A.L. Shuvalov, N.H. Scott, On singular features of acoustic wave propagation in weakly dissipative anisotropic thermoviscoelasticity, Acta Mech. 140 (1999) 1–15.
[36] V.I. Alshits, V.N. Lyubimov, Conical refraction of elastic waves in absorbing crystals, JETP 113 (2011) 659–672.
[37] K.Y. Kim, A.G. Every, W. Sachse, Focusing of fast transverse modes in (001) silicon at ultrasonic frequencies, J. Acoust. Soc. Am. 95 (1994) 1942–1952.
[38] C.-Y. Wang, J.D. Achenbach, 3-Dimensional time harmonic elastodynamic Green-functions for anisotropic solids, Proc. Roy. Soc. Lond. A449 (1995) 441.
[39] M.R. Hauser, R.L. Weaver, J.P. Wolfe, Internal diffraction of ultrasound in crystals: Phonon focusing at long wavelengths, Phys. Rev. Lett. 68 (1992) 2604–2607.
[40] R.L. Weaver, M.R. Hauser, J.P. Wolfe, Acoustic flux imaging in anisotropic media, Z. Phys. B90 (1993) 27–46.
[41] K.U. Wuerz, J. Wesner, K. Hillmann, W. Grill, Determination of elastic constants using a scanning acoustic microscope, Z. Phys. B97 (1995) 487.
[42] W. Grill, K. Hillmann, K.U. Wuerz, J. Wesner, in: A. Briggs, W. Arnold (Eds.), Advances in Acoustic Microscopy, Vol. 2, Plenum, New York, 1996, pp. 167–218.
[43] M. Pluta, A.G. Every, W. Grill, T.J. Kim, Fourier inversion of acoustic wave fields in anisotropic solids, Phys. Rev. B67 (2003) 094117-1-9.

[44] H.J. Maris, Effect of finite phonon wavelength on phonon focusing, Phys. Rev. B28 (1983) 7033–7037.
[45] A.G. Every, M. Pluta, W. Grill, Interference of non-aligned Airy diffraction patterns in acoustic microscopy images of crystals, Proc. Roy. Soc. A461 (2005) 3847–3862.
[46] A.G. Every, K.Y. Kim, Time domain dynamic response functions of elastically anisotropic solids, J. Acoust. Soc. Am. 95 (1994) 2505–2516.
[47] C.-Y. Wang, J.D. Achenbach, A new method to obtain 3D Green-functions for anisotropic solids, Wave Motion 18 (1993) 273.
[48] K.Y. Kim, L. Niu, B. Castagnede, W. Sachse, Miniaturized capacitive transducer for detection of broad-band ultrasonic displacement signals, Rev. Sci. Instrum. 60 (1989) 2785–2788.
[49] X. Zhang, J.D. Comins, A.G. Every, P.R. Stoddart, W. Pang, T.E. Derry, Surface Brillouin scattering study of the surface excitations in amorphous silicon layers produced by ion bombardment, Phys. Rev. B58 (1998) 13677–13685.
[50] A.G. Every, K.Y. Kim, A.A. Maznev, The elastodynamic response of a semi-infinite anisotropic solid to sudden surface loading, J. Acoust. Soc. Am. 102 (1997) 1346.
[51] A.A. Maznev, A.G. Every, Secluded supersonic surface waves in germanium, Phys. Lett. A197 (1995) 423–427.
[52] G.W. Farnell, in: W.P. Mason, R.N. Thurston (Eds.), Physical Acoustics, Vol. 6, Academic Press, New York, 1970, p. 109.
[53] G.W. Farnell, E.L. Adler, in: W.P. Mason, R.N. Thurston (Eds.), Physical Acoustics, Vol. 9, Academic Press, New York, 1972, p. 35.
[54] A.A. Maznev, A.G. Every, Secluded supersonic surface waves in germanium, Phys. Lett. A197 (1995) 423–427.
[55] J.D. Comins, Surface Brillouin scattering, in: Handbook of Elastic Properties of Solids, Liquids, and Gases, vol. I, Academic Press, 2001, pp. 349–378 (Chapter 15).
[56] M.G. Beghi, A.G. Every, V. Prakapenka, P.V. Zinin, Measurement of the elastic properties of solids by Brillouin spectroscopy, in: T. Kundu (Ed.), Ultrasonic and Electromagnetic NDE for Structure and Material Characterization, CRC Press, Boca Raton, 2012, pp. 539–610 (Chapter 10).
[57] X. Zhang, J.D. Comins, A.G. Every, P.R. Stoddart, Surface Brillouin scattering studies on vanadium carbides, Int. J. Refractory Metals and Hard Materials 16 (1998) 303–308.
[58] V.V. Alexandrov, T.S. Velichkina, Ju.B. Potapova, I.A. Yakovlev, Mandelstamm-Brillouin studies of peculiarities of the phonon frequency distribution at cubic crystal (001) faces, Phys. Lett. A171 (1992) 103–106.
[59] T. Wittkowski, G. Distler, K. Jung, B. Hillebrands, J.D. Comins, General methods for the determination of the stiffness tensor and mass density of thin films using Brillouin scattering: study of tungsten carbide films, Phys. Rev. B69 (2004) 205401-1-9.
[60] A.G. Every, A.A. Maznev, Ray splitting in the reflection and refraction of surface acoustic waves in anisotropic solids, J. Acoust. Soc. Am. 127 (5) (2010) 2813–2818.
[61] A.A. Kolomenskii, A.A. Maznev, Observation of phonon focusing with pulsed laser excitation of surface acoustic waves in silicon, JETP Lett. 53 (1991) 423–426.
[62] A.A. Kolomenskii, A.A. Maznev, Propagation of laser-generated surface acoustic waves visualized by shake-off of fine particles, J. Appl. Phys. 77 (1995) 6052–6054.
[63] A.A. Kolomenskii, A.A. Maznev, Phonon focusing effect with laser generated ultrasonic surface waves, Phys. Rev. B 48 (1993) 14502–14508.
[64] A.A. Maznev, A.G. Every, Formation of surface phonon focusing caustics in crystals, Solid State Commun. 97 (1996) 679–687.
[65] A.A. Maznev, A.G. Every, Focusing of acoustic modes in thin anisotropic plates, Acta Acust. 3 (1995) 387–391.
[66] B. Chapius, N. Terrien, D. Royer, Excitation and focusing of Lamb waves in a multilayered anisotropic plate, J. Acoust. Soc. Am. 127 (2010) 198–203.
[67] I. Solodov, G. Busse, Anisotropy of plate waves in composites: effects and implications, Acta Acust. United Acust. 97 (2011) 678–685.
[68] E. Glushkov, N. Glushkova, A. Eremin, Forced wave propagation and energy distribution in anisotropic laminate composites, J. Acoust. Soc. Am. 129 (2011) 2923–2934.
[69] A. Karmazin, E. Kirillova, W. Seemann, P. Syromyatnikov, A study of time harmonic guided Lamb waves and their caustics in composite plates, Ultrasonics 53 (2013) 283–293.
[70] A.G. Every, K.Y. Kim, A.A. Maznev, The elastodynamic response of a semi-infinite anisotropic solid to sudden surface loading, J. Acoust. Soc. Am. 102 (1997) 1346–1355.
[71] A.G. Every, K.Y. Kim, A.A. Maznev, Surface dynamic response functions of anisotropic solids, Ultrasonics 36 (1998) 349.
[72] Y. Sugawara, O.B. Wright, O. Matsuda, M. Takigahira, Y. Tanaka, S. Tamura, V.E. Gusev, Watching ripples on crystals, Phys. Rev. Lett. 88 (2002) 185504-1-4.
[73] T. Tachizaki, T. Muroya, O. Matsuda, Y. Sugawara, D.H. Hurley, O.B. Wright, Scanning ultrafast Sagnac interferometry for imaging two-dimensional surface wave propagation, Rev. Sci. Instr. 77 (2006) 043713-1-12.
[74] Y. Tanaka, M. Takigahira, S. Tamura, Wave-front images of acoustic waves in the (100) and (001) surfaces of TeO$_2$, Phys. Rev. B66 (2002) 075409.
[75] T. Saito, O. Matsuda, M. Tomoda, O.B. Wright, Imaging gigahertz surface acoustic waves through the photoelastic effect, J. Opt. Soc. Amer. B27 (2010) 2632.
[76] Y. Sugawara, O.B. Wright, O. Matsuda, Direct access to the dispersion relations of multiple anisotropic surface acoustic modes by Fourier image analysis, Appl. Phys. Lett. 83 (2003) 1340–1342.
[77] D.H. Hurley, O.B. Wright, O. Matsuda, T. Suzuki, S. Tamura, Y. Sugawara, Time-resolved surface acoustic wave propagation across a single grain boundary, Phys. Rev. B73 (2006) 125403.
[78] H. Kosaka, T. Kawashima, A. Tomita, M. Notomi, T. Tamamura, T. Sato, S. Kawakami, Self-collimating phenomena in photonic crystals, Appl. Phys. Lett. 74 (1999) 1212–1214.
[79] Z. Lu, S. Shi, J.A. Murakowski, G.J. Schneider, C.A. Schuetz, D.W. Prather, Experimental demonstration of self-collimation inside a three-dimensional photonic crystal, Phys. Rev. Lett. 96 (2006) 173902.
[80] D.W. Prather, S. Shi, J. Murakowski, G.J. Schneider, A. Sharkawy, C. Chen, B. Miao, R. Martin, Self-collimation in photonic crystal structures: a new paradigm for applications and device development, J. Phys. D: Appl. Phys. 40 (2007) 2635–2651.
[81] V. Espinosa, V.J. Sanchez-Morcillo, K. Staliunas, I. Perez-Arjona, J. Redondo, Subdiffractive propagation of ultrasound in sonic crystals, Phys. Rev. B76 (2007) 140302.
[82] A.J. Slobodnik, T.L. Szabo, Minimal diffraction cuts for acoustic surface wave propagation on Bi$_{12}$GeO$_{20}$, J. Appl. Phys. 44 (1973) 2937–2941.
[83] J.P. Pendry, Negative refraction, Contemp. Phys. 50 (2009) 363–374.
[84] S. Zhang, L. Yin, N. Fang, Focusing ultrasound with an acoustic metamaterial network, Phys. Rev. Lett. 102 (2009) 194301.
[85] K. Imamura, S. Tamura, Negative refraction of phonons and acoustic lensing effect of a crystalline slab, Phys. Rev. B70 (2004) 174308.
[86] I.M. Mason, Anisotropy, diffraction scaling, surface wave lenses, and focusing, J. Acoust. Soc. Am. 53 (1973) 1123–1128.
[87] A.M. Lomonosov, P. Hess, R.E. Kumon, M.F. Hamilton, Laser-generated nonlinear surface wave pulses in silicon crystals, Phys. Rev. B69 (2004) 035314-1-13.
[88] A.M. Lomonosov, P. Hess, A.P. Mayer, Silicon edges as one-dimensional waveguides for dispersion-free and supersonic leaky wedge waves, Appl. Phys. Lett. 101 (2012) 031904-1-4.
[89] T. Yanagisawa, T. Ohgi, S. Akao, N. Nakaso, Y. Tsukahara, T. Ohara, T. Tsuji, K. Yamanaka, Meandering collimated beam of surface acoustic waves on a trigonal crystal ball, Appl. Phys. Lett. 98 (2011) 123508-1-3.